A coarse-grained model of affinity maturation indicates the importance of B-cell receptor avidity in epitope subdominance

Victor Ovchinnikov [1,*] **and Martin Karplus** [1,2,*]

[1] *Department of Chemistry and Chemical Biology, Harvard University, Cambridge, MA, 02138, USA*

[2] *Laboratoire de Chimie Biophysique, ISIS, Université de Strasbourg, 67000 Strasbourg, France*

Correspondence*:
Victor Ovchinnikov, 12 Oxford St, Department of Chemistry and Chemical Biology, Cambridge, MA, 02138, USA
ovchinn@fas.harvard.edu or ovchinnv@georgetown.edu

Martin Karplus, 12 Oxford St, Department of Chemistry and Chemical Biology, Cambridge, MA, 02138, USA, marci@tammy.harvard.edu

ABSTRACT

The elicitation of broadly neutralizing antibodies (bnAbs) is a major goal in the design of vaccines against rapidly-mutating viruses. In the case of influenza, many bnAbs that target conserved epitopes on the stem of the hemagglutinin protein (HA) have been discovered. However, these antibodies are rare, are not boosted well upon reinfection, and often have low neutralization potency, compared to strain-specific antibodies directed to the HA head. Different hypotheses have been proposed to explain this phenomenon. We use a coarse-grained computational model of the germinal center reaction to investigate how B-cell receptor binding valency affects the growth and affinity maturation of competing B-cells. We find that receptors that are unable to bind antigen bivalently, and also those that do not bind antigen cooperatively, have significantly slower rates of growth, memory B-cell production, and, under certain conditions, rates of affinity maturation. The corresponding B-cells are predicted to be outcompeted by B-cells that bind bivalently and cooperatively. We use the model to explore strategies for a universal influenza vaccine, *e.g.*, how to boost the concentrations of the slower growing cross-reactive antibodies directed to the stem. The results suggest that, upon natural reinfections subsequent to vaccination, the protectiveness of such vaccines would erode, possibly requiring regular boosts. Collectively, our results strongly support the importance of bivalent antibody binding in immunodominance, and suggest guidelines for developing a universal influenza vaccine.

Keywords: germinal center, simulation, influenza, hemagglutinin, vaccination

1 INTRODUCTION

Viral respiratory infections remain a high source of morbidity and mortality around the world. Universal vaccines against highly-mutable viruses such as influenza and HIV are therefore highly desirable. However,
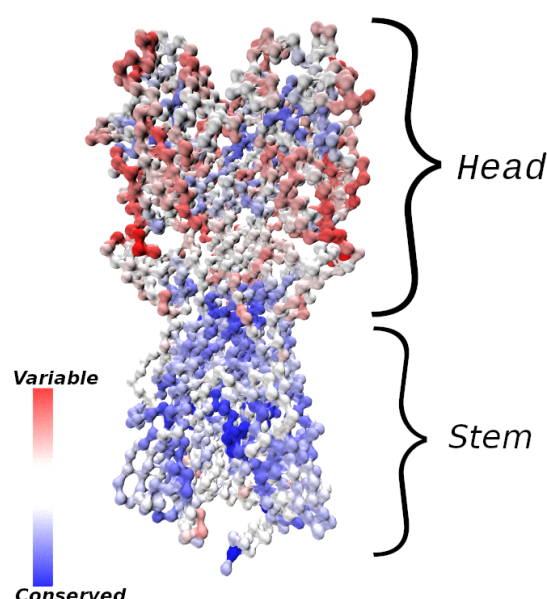
Figure 1. Influenza hemagglutinin (HA) spike protein colored by residue conservation. Sequences of avian, swine and human influenza type A spike proteins spanning the years 1918–2019 and subtypes 1-18 were downloaded from the NIH influenza research database(3); conservation was computed in MATLAB(4) after clustering the sequences to 97% identity and multiple alignment. The HA structure was taken from PDB entry 3LZG(5), and the image was generated using Visual Molecular Dynamics.(6) Only the C_α atoms are shown.

their development is complicated by the high antigenic drift of the viral genomes, which stems from low replicative fidelity of viral nucleic acid polymerases. In the case of influenza, there also exists the possibility of antigenic 'shifts', whereby genome segments from different viral strains are reassorted in a host co-infected with multiple viruses. Such reassortments can result in pandemic strains against which preexisting immunity in the affected population is low. For example, the H1N1 1918 influenza pandemic was likely caused by a reassortment between avian and human influenza strains, the 2009 H1N1 pandemic was probably caused by a triply reassorted human, avian, and swine strain,(1) and the SARS-CoV2 pandemic is believed to have originated from a bat virus adapted to infect humans and other hosts.(2)

Despite the high mutation potential of many viruses, epitopes that are relatively well conserved between different strains, and antibodies that bind to them, have been discovered. In the case of the influenza hemagglutinin (HA) protein (see Fig. 1), the majority of conserved epitopes are located on the stem or base of the HA(7, 8); less frequently, they are found in the HA head, *e.g.*, at the interface between the heads of HA monomers(9, 10) in a homotrimer, or in the vicinity of the sialic acid receptor(11, 12). There are different plausible reasons for the increased sequence conservation of these regions, such as (i) maintenance of function (*e.g.* the sialic acid receptor is required for host cell entry, and properly folded and probably somewhat rigid HA helices are needed for fusion with the host cell) and (ii) a lack of evolutionary pressure to drive escape mutants(11); the stem epitopes and the occluded epitope(9) are less accessible to antibodies, and thus experience less selective pressure than the exposed HA head. Because antibodies (Abs) that bind conserved epitopes could confer protection against many different viral strains, the elicitation of such cross-reactive, or broadly-neutralizing Abs (bnAbs) has been a goal of vaccine development.(7) BnAbs have been isolated from animal and human subjects in response to natural infection or vaccination,(8) and some have been engineered(13) to have very high breadth, providing simultaneous protection against phylogenetically distant group I and II HAs.(14, 15, 13) We note, however, that strong sequence or

46 structural conservation of epitopes shared by different antigens is not an absolute requirement for
47 targeting by bnAbs, as many polyreactive and self-reactive bnAbs have been discovered that are
48 able to bind divergent ligands through structural flexibility.(16, 17)

49   Unfortunately, bnAbs tend to be rare and are not well boosted in infections(15, 18, 19, 20). Further, most
50 of them have lower neutralization potency, compared to strain-specific Abs. However, bnAbs have different
51 mechanisms of protection, *e.g.* labeling infected cells for destruction by Ab-directed cytotoxicity (ADCC),
52 or inhibiting membrane fusion after phagocytosis by the host cell,(7) rather than blockage of viral binding
53 to cells, so that direct comparisons between different Abs are not always informative. Many bnAbs have
54 been shown to provide heterosubtypic protection in passive immunization studies,(8) indicating that their
55 elicitation by a vaccine could provide broad immunity. In the case of influenza, titers of stem-directed Abs
56 have been shown to increase with age, correlating inversely with incidence of symptomatic infection.(21)

57   The antigenic epitopes targeted by rare bnAbs are labeled immunosubdominant, because they usually
58 are not the primary targets of immune responses. Since durable vaccine responses against highly-mutable
59 pathogens will need to overcome immunodominance, *i.e.* to focus on conserved subdominant epitopes,
60 various possible causes for subdominance have been considered. They include (i) epitope autoreactivity,(12)
61 (ii) low frequency of germline precursor antibodies able to bind the epitopes in question,(22) also
62 described as "holes" in the human antibody repertoire, which HIV exploits to protect its conserved
63 regions(23), (iii) epitope shielding by glycans,(10) (iv) preexisting immune memory,(22, 20) poor steric
64 accessibility of epitopes(24), (v) inability to recruit sufficient T-cell help in germinal centers (GCs) due to a
65 lack of compatible MHCII (major histocompatibility complex of type 2) epitopes,(19) and (vi) entropic
66 dominance of distracting epitopes.(25, 24, 26) Although multiple effects are likely to contribute, it is of
67 interest to identify the most important ones. In the context of influenza HA, especially in regard to the
68 stem and the occluded interfacial epitope of Watanabe et al. (9), low steric accessibility appears to be a
69 particularly important factor.

70   Andrews et al. (22) found that some stem-directed Abs bound virus particles with an affinity that was
71 an order of magnitude lower than that for recombinant HA, which was interpreted in terms of reduced
72 accessibility of stem epitopes of whole virions. Harris et al. (27) used cryo-electron tomography
73 (cryo-ET) to estimate the average spacing between HA spikes on influenza virions at 14nm,
74 which appears to be compatible with bivalent binding of antibodies to the HA stem, based on
75 the docking of an unrelated mouse IgG antibody.(27) However, although the study demonstrated
76 that stem epitopes are accessible to antibodies, because of rotational averaging, only one Fab of
77 a stem antibody could be placed based on the cryo-ET data; the authors suggested that steric
78 constraints may lower binding stoichiometry. Amitai et al. (24) used molecular simulations to map the
79 accessibility of HA epitopes to antibody binding on model virus-like particles (VLPs), and predicted that
80 the rate of bivalent (avid) antibody binding to stem epitopes is much lower than that for head epitopes. The
81 importance of bivalent binding in antibody maturation was demonstrated elegantly by Kanekiyo et al. (28),
82 who co-displayed HA receptor binding domains (RBDs) from different influenza strains on nanoparticles
83 (NPs). The heterotypic NPs (RBDs from multiple strains on an NP) elicited Abs with higher breadth than a
84 mixture of homotypic NPs (RBD from a single strain on an NP). Because the vaccines differed only in
85 the geometric arrangement of the antigens, and not in composition or proportion, the results imply that
86 mosaic display confers an advantage to cross-reactive Abs *via* bivalent binding(28). Similar results were
87 obtained recently for the SARS-CoV2 RBD.(29) The importance of multivalent antigen binding in
88 affinity maturation was also shown in the discovery of vaccine-induced Fab-dimerized antibodies
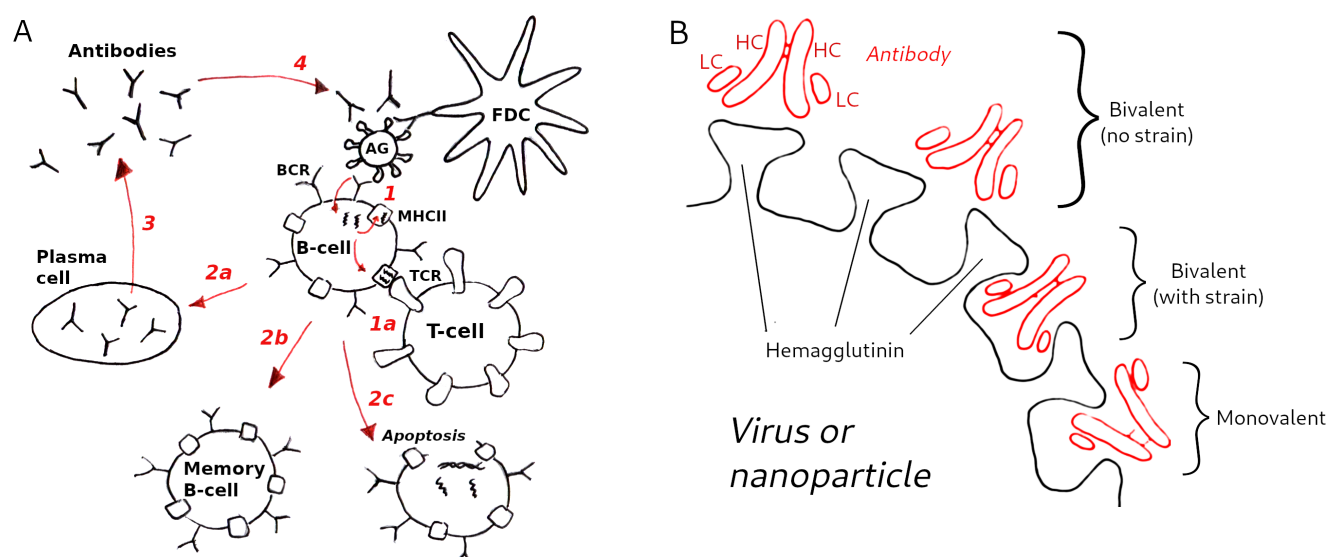89 directed to HIV glycans.(30)

Figure 2. Schematic of the GC model used in this study. (A) Model overview: (1) B-cells are activated upon binding to antigen presented on follicular dendritic cells (FDCs, not explicitly modeled); (1a) in the optional T-cell help model (see text) B-cells are activated when the major histocompatibility complex receptor (MHC2) binds to the T-cell receptor (TCR); B-cell activation rescues B-cells from apoptosis, allowing them to mutate and proliferate; (2) depending on the activation signal, B-cells can differentiate to plasma cells (2a), to memory B-cells (2b), or undergo apoptosis (2c); (3) Plasma cells secrete antibodies (Abs), which also compete with B-cell receptors for antigen (4), which is the essential aspect of the Ab feedback model(31) (see text). (B) Hypothetical modes of antibody binding to influenza spikes; bivalent binding without strain (top) corresponds to cooperative binding by antibody arms; bivalent binding with strain (middle) corresponds to noncooperative binding; monovalent binding (bottom) is assumed to be the dominant mode of binding of anti-HA stem antibodies (see Methods for details).

90   Motivated by these studies, we employed a coarse-grained computer model of affinity maturation (AM)
91 in GCs to investigate how avidity differences in the binding of B-cell receptors (BCRs) to their cognate
92 antigens (AGs) could influence the patterns of immunodominance observed experimentally. Despite the
93 coarse-graining, the model allows comparisons between multiple competing epitope/paratope pairs, in
94 terms of B-cell and Ab production and affinity for antigen. We first show that the model is in qualitative
95 agreement with experimental observations of the basic properties of GC reactions, and of the subdominance
96 of influenza stem epitopes, whose predominant mode of binding to BCR/Ab is assumed to be monovalent.
97 We then use the model to simulate multiple exposures to an antigen and interpret the results to propose
98 strategies for overcoming immunodominance. We suggest that bnAbs that target subdominant epitopes are
99 most likely to be elicited by increasing effective epitope concentration *via* design of custom immunogens
100 or cocktail composition. The present model also predicts the resulting immune memory to be short-
101 lived, which suggests that regular boosts may be required for vaccines composed of immunosubdominant
102 epitopes.

103   Because the model and its computer implementation involve many technical aspects, we include the
104 detailed Methods section at the end of the paper, after the Results and Discussion, which are presented
105 next.

2 RESULTS

A visual schematic of the model is given in Fig. 2, and a brief overview is presented below. Complete details of the model equations and parametrization are given in Methods, and the parameter values used are listed in Table 1. Our approach is related to the differential equation models of Kepler and Perelson (32) and listed Oprea and Perelson (33). These models achieve a balance between biological detail and computational complexity: (i) they are sufficiently accurate to model the population sizes of B-cell receptors (BCRs) with different affinities, represented by discretized affinity classes; (ii) they contain a relatively small number of parameters, and (iii) they are simple enough to permit a large number of simulations to study the effects of different initial conditions or model parameters.(32, 33) More sophisticated approaches exist, which model individual interactions between immune complexes (ICs), Ags, BCRs and T-cells, aiming to capture GC reactions in higher detail.(34, 35) However, their use would be computationally prohibitive for this study. For example, modeling the case in which the initial BCR affinity to an antigen was drawn randomly from a distribution involved 8400 germinal center simulations, each 35 days in duration (see Results).

As in other models of affinity maturation,(36, 37) the interaction between BCRs and AGs is represented by a Langmuir isotherm that uses two equilibrium association constants, which represent binding of the first and second antibody arm. Unlike the more detailed models,(38, 24) the present model does not have an explicit structural component, and the effect of bivalency is reflected in the assignment of the association constants. Further, we simplify the biology by not distinguishing between centroblasts and centrocytes, nor between light and dark zones (LZ *vs.* DZ). Instead we consider the overall proliferation and death rates. This choice is motivated by the findings that the differences between centroblasts and centrocytes, and, more generally between the LZ and DZ, are smaller than previously thought;(39) *i.e.*, the physical boundary between LZ and DZ is rather diffuse, selection and proliferation can occur in both zones, albeit with different rates, and T-helper cells appear to be present in both zones, albeit in different proportions. Because we are interested in the dependence of the immune response on the number of competing BCRs with different binding valency and affinity, the model is parametrized to predict the following quantities: (i) the number of GC B-cells, (ii) the number of memory B-cells (MBCs), some of which can be recruited into secondary GCs, (iii) the number of plasma cells (PCs) that secrete Abs, (iv) the number of Abs, which compete with BCRs for antigen and implicitly regulate GC size,(31) and, optionally, (v) the T-helper cell population (which is discussed in SI Appendix). The species (i)–(iv) are distributed into affinity classes, while the T-cell model uses two equilibrium affinities, those between TCRs and MHCIIs loaded or unloaded with peptides. The T-cell model is related to the T-cell expansion model of Mayer et al. (40). We consider the model to be optional for the simulations performed here, because qualitatively the same results were obtained by assuming that the amount of T-cell help is equal to BCR activation by binding to antigen. However, the reason for the similar results obtained here could be the simplicity of our model, as we did not consider multiple distinct T helper cell populations, which were shown to be important for bnAb elicitation in a recent computational study.(41) Thus, in the main text, we present simulation results obtained without an explicit T-cell model. However, several validation calculations performed with the model are described in SI Appendix.

We first show that the model captures some experimentally determined properties of GCs. In Fig. 3 we compare the model results obtained with a single BCR/Ag pair to the average GC size reported by Wittenbrink et al. (42), and the MBC and PC production rates determined by Weisel et al. (44). The experimental data were also used by Pélissier et al. (43) to parametrize their stochastic GC model, which was used to explore the mechanism of clonal bursts. We note that the Wittenbrink et al. (42) observed very high CG size variability, as reflected in the experimental error bars (Fig. 3); thus, the agreement between
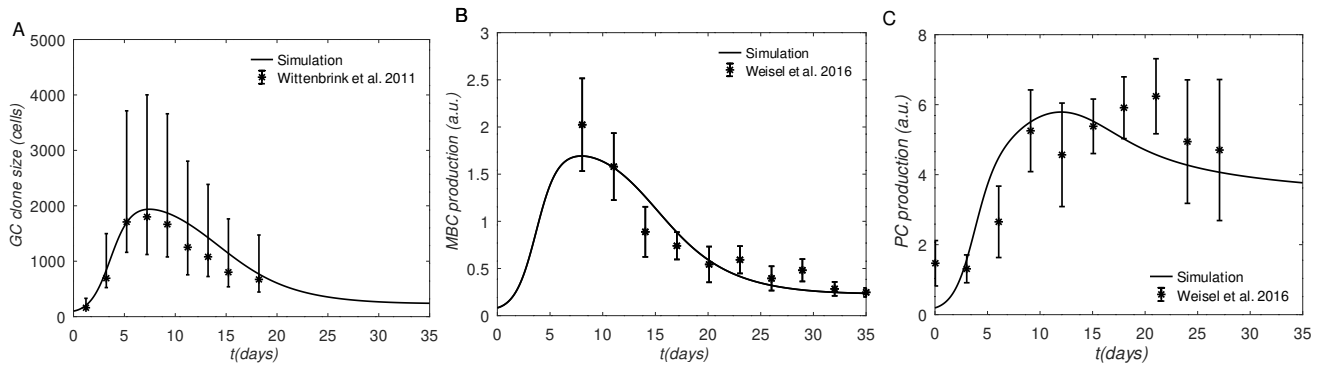
Figure 3. Comparison of simulation and experiments. A: Total B-cells, B: Memory B-cell production rate, C: Plasma cell production rate. Experimental data for panel A was generated from the GC cross-sectional areas plotted in Fig. S1B of Ref. 42, and converted to B cell counts as done in Ref. 43; The lower and upper error bars in panel A correspond to 30% and 70% quantiles, respectively; experimental data for panels B & C were taken from Fig. 4 of Ref. 43, who obtained raw data from Weisel et al. (44); the error bars in B & C correspond to approximately one SD, estimated from the range of the data, which we assumed to be Gaussian-distributed.

149 our model and the experimental average should be considered as a qualitative validation, as the model does
150 not capture GC size heterogeneity.

151   One apparent disagreement is that rate of PC production in our model is accelerated by several days,
152 compared to the data of Weisel et al. (44) (see Fig. 3C). Although the experimental MBC and PC production
153 in Fig. 3B & C, respectively, correspond to the same time, matching the PC production rate in the simulation
154 required shifting the experimental measurements by several days (compare Fig. 3B with Fig. 3C). However,
155 the discrepancy is not expected to affect our results significantly, because we are interested in comparing the
156 relative MBC output from different lineages at the end of GC reactions, which are simulated consistently,
157 *i.e.* using the same model.

158   Next, we investigate the effects of BCR binding avidity under different scenarios. First, we compare
159 the growth rates of three noncompeting B-cell lineages, which differ only in the value of the second-arm
160 equilibrium binding constant K_{eq}^2 (written as K^{i2} for lineage i in Eq. (4) of Methods). This idealized
161 scenario corresponds to three GCs evolving independently, which is the noninteracting, $o=0$, case (see
162 Methods, Sec. 4.0.5), each completely dominated by a single B-cell lineage.

163   We compare the behavior of lineages with three regimes of bivalency, corresponding to $K_{eq}^2=0$, $K_{eq}^2=K_{eq}^1$,
164 and $K_{eq}^2=10K_{eq}^1$, which we denote, respectively, as the monovalent, noncooperative, and cooperative
165 binding cases. The justification for the chosen values is discussed in the Methods Sec. 4.0.2.

166   The results in Fig. 4A show that the monovalent BCR has a significantly slower rate of growth compared
167 with the bivalent BCRs, due to the reduced activation by Ag assumed by the model. In the monovalent case,
168 the maximum B-cell count is less than a third of that in the bivalent cooperative case, and less than half of
169 that in the noncooperative case; this lower maximum is also reached later; *i.e.*, after 20 days, *vs.* 5 to 7 days.
170 Further, the MBC count at the end of the GC is reduced by half in the monovalent case, compared with
171 the cooperative case (Fig. 4B), and the final average affinity of the B-cell population is several-fold lower
172 (Fig. 4C). The delayed peak in the monovalent response is qualitatively consistent with the observations of
173 Tan et al. (19), who noted that the anti-influenza stem Ab response was delayed by a week relative to the
174 overall Ab response, and that the B-cell response was several-fold lower in magnitude.
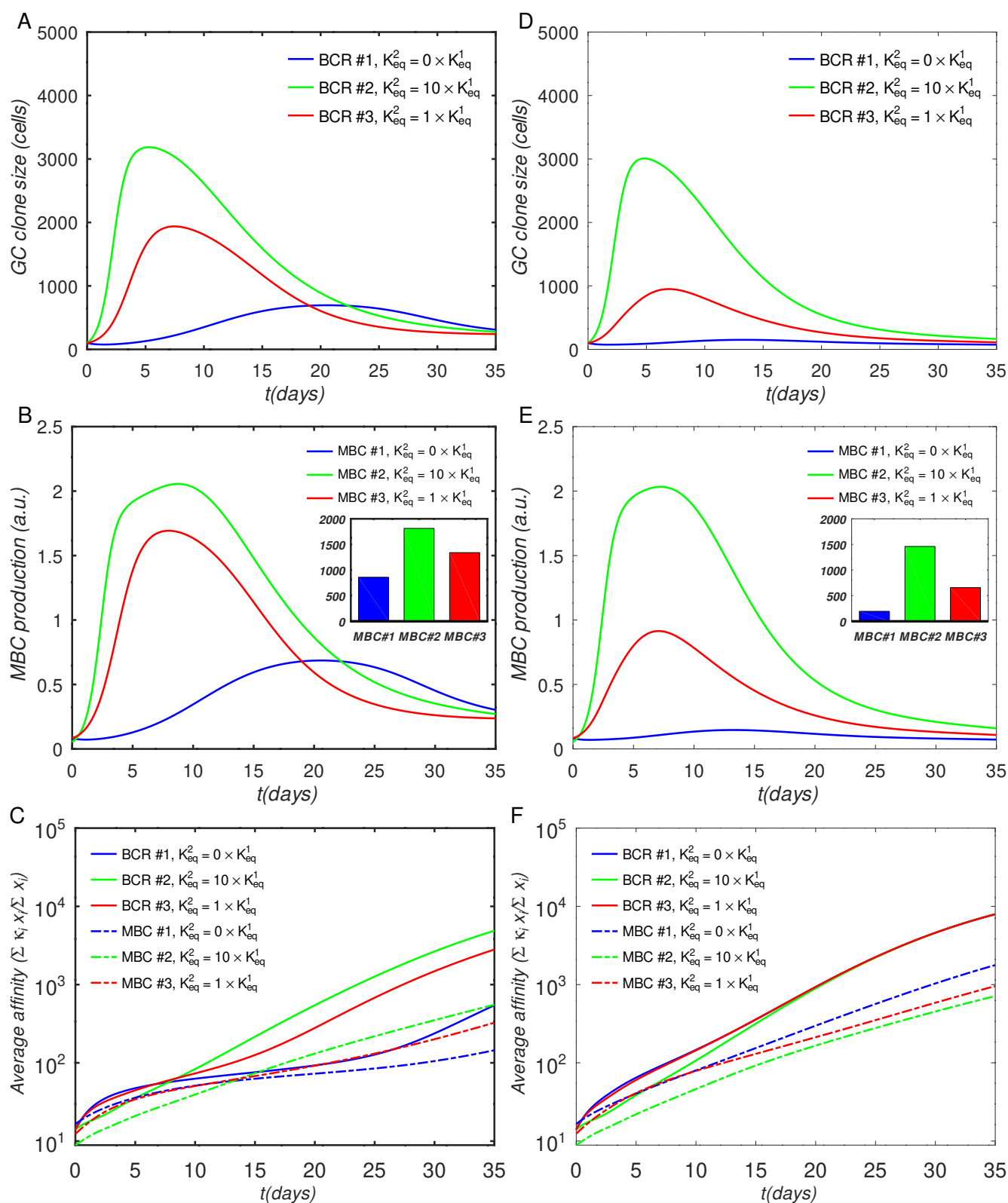
Figure 4. Effect of antibody valency and epitope occlusion on GC properties. Left column (A–C): noninteracting B-cell case ($o = 0$); Right column (D–F): fully interacting B-cell case ($o = 1$); A,D: Total B cells; B,E: Memory cell production rate; insets: total MBC population at end of simulation; C,F: Average affinity of B-cells and MBCs. For the definition of occlusion o, see Sec. 4.0.5.

175   Although the noninteracting GC case is illustrative, it is idealized, because in affinity maturation there
176 will generally be many different B-cell lineages competing for epitopes on the Ags, or for T-cell help
177 signals. Thus, a more realistic model of a single GC needs to account for competition between different
178 lineages. As described in Sec. 4.0.5 we model this competition using an *occlusion* parameter o, with $o = 0$
179 for the fully noninteracting case, presented above, and $o = 1$ for the fully interacting (competing) case. We
180 note that a similar approach to model clonal competition was used by Yan and Wang (45), who
181 introduced interaction parameters to represent Ag binding interference from Abs produced by
182 earlier generations of B-cells.

183   We describe the results of the fully interacting case (o=1) next; however, we note that a more realistic
184 description of the overall GC reaction would probably involve intermediate values of o. For example, if,
185 in some cases, different B-cells are able to bind to different epitopes on the same Ag simultaneously, the
186 occlusion parameter would need to be less than 1, which would correspond to decreased competition
187 between the B-cells. Moreover, when modeling multiple GCs, it may be necessary to include the possibility
188 that the Abs secreted by the plasma cells can diffuse across many GCs, and compete with the 'local' BCRs
189 for Ag.(31) This scenario would correspond to indirect competition between different B cell lineages in
190 different GCs, which might be modeled with some optimized intermediate (though generally unknown)
191 occlusion value. A possible starting point for estimating such a value could involve competitive binding
192 experiments using antibodies specific for the different epitopes.

193   The simulation of the fully interacting case shows that the population disadvantage of the monovalent
194 lineage is further increased (Fig. 4)D–F. The peak B-cell concentration of the monovalent lineage is more
195 than 10-fold lower than that of the bivalent cooperative lineage (panel D). These results are to be expected,
196 because the more rapidly proliferating lineage occludes the Ag, effectively reducing the amount of epitope
197 available to the the monovalent lineage. The average monovalent MBC production is lower by about a
198 factor of eight relative to the bivalent cooperative case (panel E).

199   It is noteworthy that the average affinities of the three BCRs are indistinguishable after about 20 days
200 after initiation of the GC reaction in the fully competing case (panel F). Further, the BCR affinities in this
201 case at the end of the simulation are higher than those in the o=0 case (Fig. 4C *vs.* Fig. 4F). This result is
202 understandable in terms of increased competition for survival inside the interacting (o=1) GC. The fact
203 that binding by one BCR occludes access to other epitopes implies that the effective epitope availability
204 is decreased for all BCRs. A decrease in the available binding sites increases the selection pressure on
205 the BCRs, leading to the survival of the higher-affinity lineages. We will return to this point when we
206 investigate the effects of varying epitope concentration explicitly. For completeness, simulation results
207 with intermediate values of occlusion are shown in Fig. S1.

208   As discussed in the introduction, the reason for targeting immunosubdominant epitopes such as the
209 influenza HA stem or the interfacial epitope(9) in vaccinations is their association with the elicitation of
210 bnAbs, which are likely to provide protective immunity against future strains. In the context of the present
211 simulations, such pre-existing protective immunity can be modeled by increasing the initial affinity of the
212 monovalent antibodies, while keeping the other affinities unchanged. This gives the monovalent antibodies
213 a survival advantage. A physiological rationale of setting a higher initial affinity of monovalent Abs could
214 be that a significant proportion of monovalent (*e.g.*, anti-HA stem) MBCs are recruited into secondary
215 GCs, where the higher initial affinity allows the MBC-derived blasts to compete more effectively with
216 naïve bivalent B-cells. A recent study comparing the early plasmablast (PB) response with GC B
217 cells obtained by fine-needle aspiration from vaccinated human subjects, found a variable, and
218 sometimes large, clonal overlap (12% - 88%) between B cells in the PB pool and those in the GC,
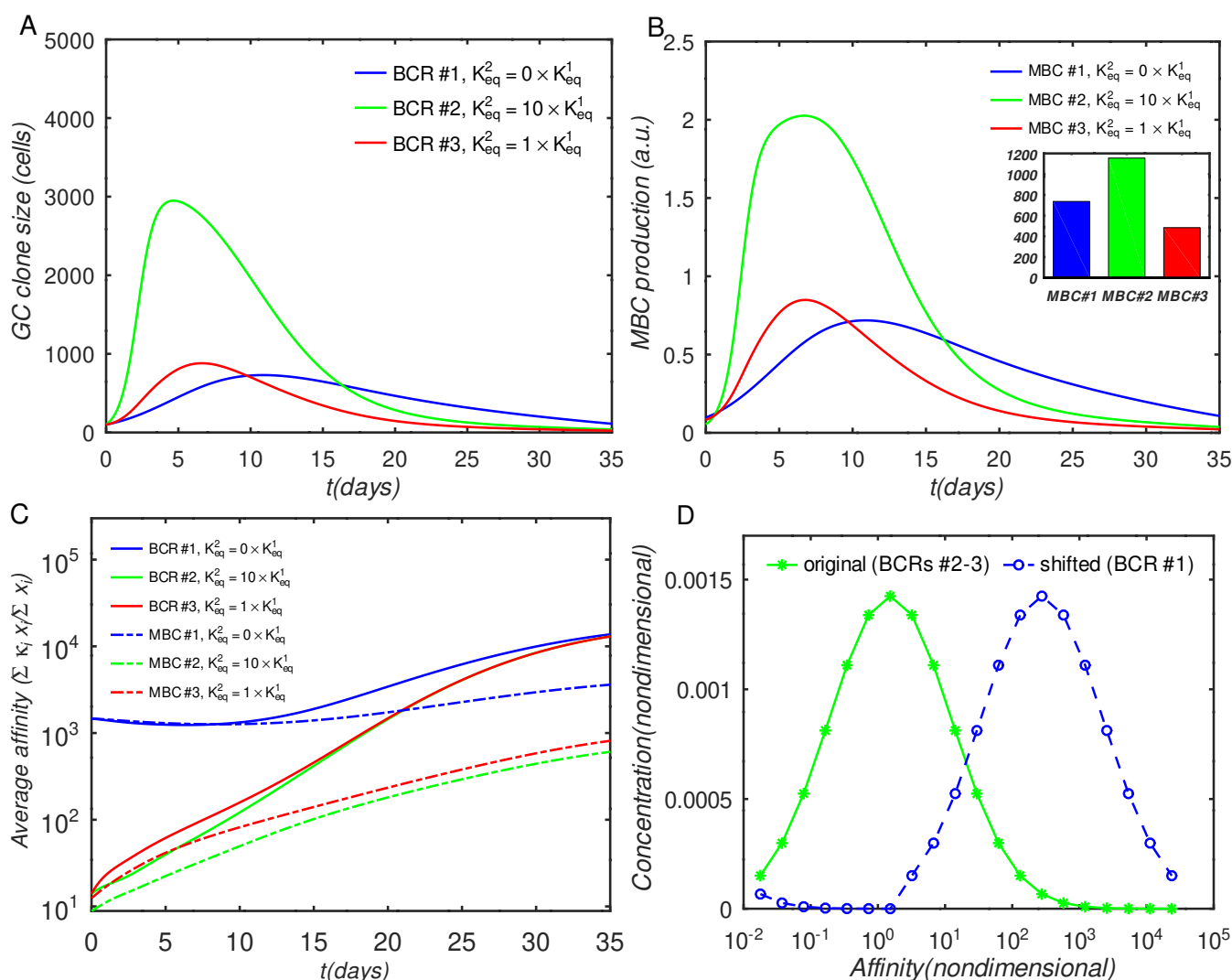
Figure 5. Effect of initial affinity advantage on the growth of monovalent B-cells in the fully interacting B-cell case ($o = 1$). Panels A–C show the same quantities as Fig. 4A–C; The affinity distribution corresponding to BCR#1 was shifted toward higher values relative to BCR#2 and BCR#3 (panel D).

219 suggesting that substantial recruitment of MBCs into GCs is possible.(46) To model this scenario,
220 we shifted the initial affinity distribution of the monovalent Abs by about two orders of magnitude towards
221 higher values (see the distributions in Fig. 5D), and repeated the simulations for the fully interacting o=1
222 case (the o=0 case is shown in Fig. S2).

223 Figure 5A shows that the population of the monovalent B-cells increased several-fold as compared
224 with Fig. 4D (no advantage), such that, at their peak, these B-cells were almost as numerous as the
225 bivalent noncooperative ones. However, even the large affinity advantage was insufficient to overcome
226 the dominance of the cooperatively-binding Abs in terms of the total MBC response, which was still
227 significantly lower in the monovalent case (Fig. 5B). Nachbagauer et al. (47) found that anti-HA stem
228 immunity can be elicited or boosted upon immunization with chimeric HA constructs with HA heads
229 to which the host is naïve, fused to HA stems against which there is preexisting immunity. In other
230 studies,(48, 18) it was reported that boosting with HAs from pandemic, rather than with seasonally-drifted
231 strains, boosted anti-stem immunity more effectively. The authors' interpretation of the results was that the
232 vaccinations boosted preferentially anti-stem responses derived from MBCs, which were able to outcompete

233 the naïve response to the HA head. Further, Ellebedy et al. (18) also found that immunosubdominance of
234 the stem reemerged after repeat immunization with the same pandemic strain.

235   To test whether the above findings could be explained with the present model, we systematically repeated
236 the preceding simulations for different numbers of distinct BCR/epitope pairs (2 to 15), different occlusion
237 values o=[0,0.5,0.9,1], and three different values of affinity advantage provided to BCR#1 (given below);
238 BCR#1 bound monovalently (K_{eq}^{12}=0) or bivalently (K_{eq}^{12}=$10K_{eq}^{11}$). The remaining BCR#i ($2 \leq i \leq 15$)
239 were modeled as bivalent with K_{eq}^{i2}=$10K_{eq}^{11}$. These simulations are discussed below, and their results are
240 shown in Fig. 6.

241   The goal of the simulations is to approximate conditions in which one monovalent or bivalent anti-stem
242 BCR (#1) lineage is evolving concurrently with 1-14 bivalent anti-head BCRs. In the first vaccination,
243 all BCRs start from the same affinity distribution peaked at $K_{eq}^1 \simeq 1.53$ (Fig. 5D). To model the effect of
244 stem conservation after the first vaccination, BCR#1 is given a (multiplicative) affinity advantage over the
245 remaining BCRs of ΔK_{eq}=10, 100, or 1000. After the first (prime) simulation, each boost is initialized with
246 a combination of 25% MBCs taken at the end of the previous simulation, and 75% naïve B-cells having
247 the same initial distribution as that used for the prime. We assume that the previously-generated anti-head
248 MBCs are poorly matched to the boosting Ag and shift their affinity distribution toward lower values
249 by a factor of 1000, essentially eliminating any advantage of previous maturation. For the presumptive
250 stem-directed BCR#1, we assume that the previously-generated MBCs are better matched to the boosting
251 Ag, and shift their affinity downward only by a factor of 100, 10, or 1 (unchanged), to explore the effect of
252 the mismatch; (thus, the affinity advantage ΔK_{eq} of BCR#1 corresponds to 1000 divided by 100, 10, or
253 1). We found that the proportion MBC#1 reaches a plateau by about five immunizations (see Fig. S3). In
254 Fig. 6 we show the fraction of MBCs#1 after the sixth simulation.

255   First, we discuss the results of the cooperative bivalent anti-stem case (Fig. 6A). Here, BCR#1 does not
256 have an avidity disadvantage (since it is cooperatively bivalent with K_{eq}^{12}=$10K_{eq}^{11}$), relative to the remaining
257 BCRs, and has an affinity advantage, as described above. In the noncompeting case (o=0) the MBC fraction
258 ζ=$MBC_1/\sum_{i=1}^{N_B} MBC_i$ is not very sensitive to the affinity advantage, because the Abs are maturing
259 independently and the concentration of each epitope is the same. As the competition between the BCR
260 lineages is increased, the affinity advantage becomes more important. For example, in the high occlusion
261 cases $o \geq 0.9$, with 9 competing low-affinity BCRs, a 1 to 3 order of magnitude affinity advantage results
262 in ~20% to ~50% of the final MBC population being derived from BCR#1 ($\zeta \in [0.2, 0.5]$ in the two right
263 panels of Fig. 6A).

264   In contrast, the monovalent anti-stem response (Fig. 6B) produces markedly lower, though still significant
265 MBC#1 proportions. For the lowest initial affinity advantage ($\times 10$), the proportion of MBC#1 is vanishingly
266 small for all interacting cases. For the higher advantage values ($\times 100$ and $\times 1000$), the proportion of MBC#1
267 with 9 competing low-affinity BCRs at $o \geq 0.9$ is in the range ~10% − ~30% ($\zeta \in [0.1, 0.3]$ in the two
268 right panels of Fig. 6B).

269   We interpret these results to suggest that a previous response to a conserved epitope could be boosted
270 to dominate the subsequent response, even in the presence of a significant number of poorly-conserved
271 'distracting' epitopes. This is consistent with the chimeric vaccination results of Nachbagauer et al. (47).
272 However, the extent of boosting is critically dependent on the affinity advantage of the preexisting immunity.
273 In the case of monovalent antibodies, the affinity advantage needs to be high to overcome the proliferation
274 disadvantage caused by monovalency, and the entropic disadvantage caused by distracting epitopes that
275 generally outnumber conserved ones. Ellebedy et al. (18) noted that vaccination with a pandemic strain
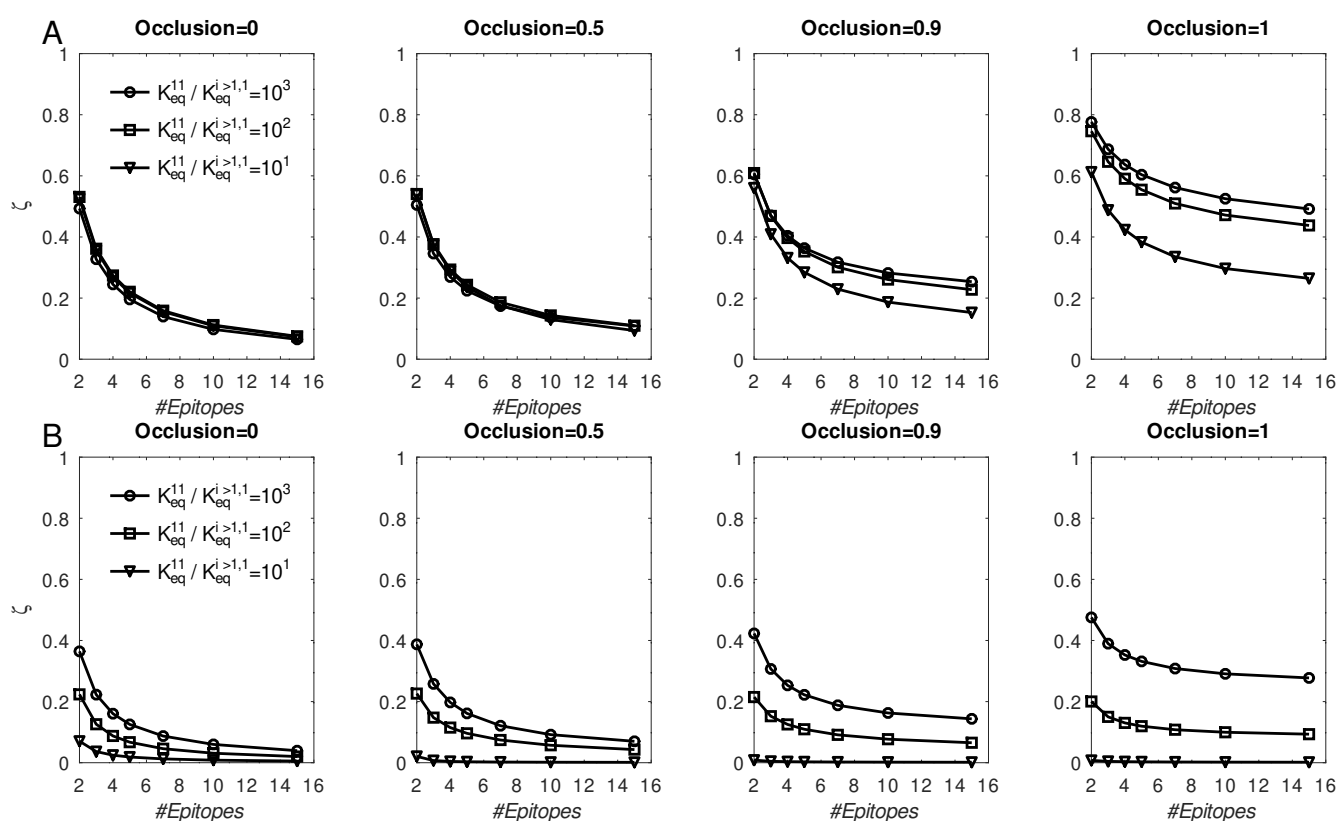
Figure 6. Fraction of MBC#1 (ζ, defined in the text) at the end of six GC simulations for different initial affinity advantage values *vs.* total number of BCR/Epitope pairs. A: BCR#1 is cooperatively bivalent ($K_{eq}^{12}=10K_{eq}^{11}$); B: BCR#1 is monovalent ($K_{eq}^{12}=0$).

276 against which anti-HA head immunity is low, preferentially boosted anti-HA stem antibodies. However,
277 upon reimmunization with the same antigen, the anti-HA head Abs were boosted preferentially. These
278 results can be rationalized in the present model by the differential affinity advantages of the anti-HA stem
279 Abs. Specifically, for the first immunization, the anti-stem immunity has a sufficient affinity advantage
280 to overcome the growth-related and entropic disadvantages. For the second immunization, the affinity
281 advantage is eroded because the anti-HA head immunity has undergone affinity maturation caused by the
282 first immunization, which leads to the restoration of stem epitope subdominance.

283 Because the affinity advantage of a conserved epitope cannot be predicted accurately if antigenic drift is
284 present, a more realistic approach would be to treat ΔK_{eq} as a random variable. To investigate this scenario,
285 we performed a round of simulations in which ΔK_{eq} was sampled from the lognormal distribution; the
286 results are described in SI Appendix S1. The differences between the two cases were similar to those in the
287 simulations with fixed ΔK_{eq}. For example, in the bivalent case, some MBC#1 cells were always present,
288 while in some simulations of the monovalent case the MBC#1 proportion is near zero (see Fig. S4).

289 The above simulations suggest that an affinity advantage alone will not always be sufficient to overcome
290 the disadvantage of slower proliferation and entropic distraction. This result, together with other factors,
291 such as low germline precursor frequency or T-cell help insufficiency,(19) could explain the lower
292 prevalence of anti-HA stem immunity.

293 In natural infections, the epitope concentrations are predetermined by the Ag itself (*e.g.*, the solvent-
294 accessible surface area of the HA head on an influenza virion is about twice that of the stem; see Fig. S5 in
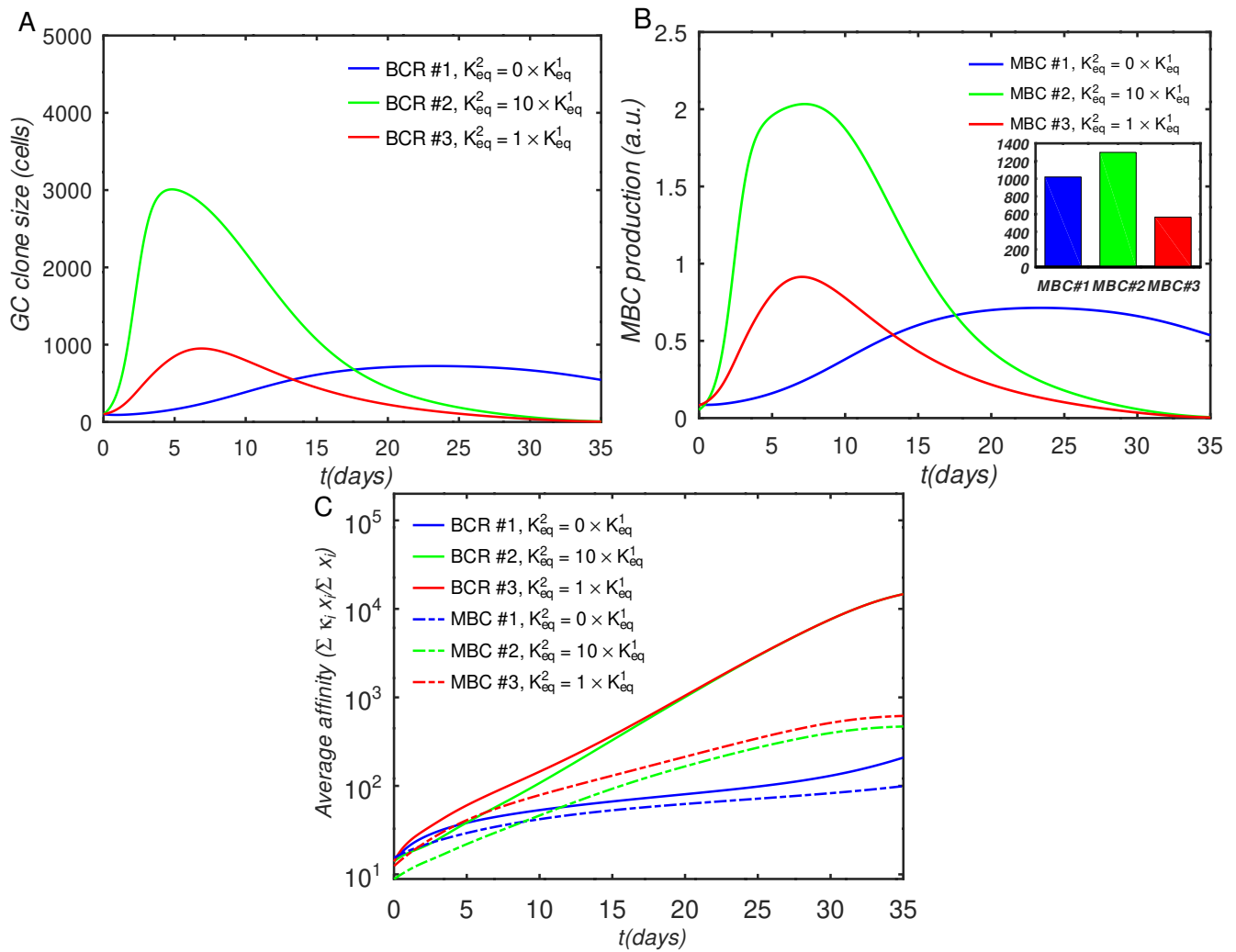
Figure 7. Effect of BCR valency and epitope concentration on GC evolution, with $o = 1$ (fully competitive case). Panels A–C show the same quantities as Fig. 4A–C; $\alpha_1^T = 2$, $\alpha_2^T = 1$, $\alpha_3^T = 1$; α^T is the nondimensional total Ag concentration (see Sec. 4.0.6).

295 SI Appendix S2). However, the vaccination setting allows use of designed antigens with some epitopes
296 masked by glycosylation(10, 49, 50) or even completely removed using protein engineering(51, 52).
297 Additionally, one can administer concurrently multiple Ags, in which some Ag epitopes are sufficiently
298 conserved between the antigens that they can be considered to represent a single epitope with a higher
299 effective concentration. (28, 53, 29, 26). In the next set of simulations, we investigate the interplay of
300 epitope concentration and BCR binding valency. Figure 7 shows the results of a GC simulation involving
301 three competing BCR/Ag pairs, for comparison with the previous 3-BCR simulations (Figs. 4 and 5);
302 the noninteracting case can be found in Fig. S6. The concentration of Ag#1, which corresponds to the
303 monovalent BCR#1, was twice that of the other two Ags, while all other parameters were the same as in
304 the original 3-BCR simulation. The peak monovalent B-cell population increases several-fold relative to
305 the uniform concentration case (Fig. 4D); it is similar in magnitude to that in the affinity-advantaged case
306 of Fig. 5, but occurs later, at ~23 *vs.* ~11 days. This behavior was expected, because, although BCR#1
307 has an impaired growth rate due to monovalency, it also has more antigen available, allowing it to grow
308 for longer times. Even though the other (bivalent) BCRs are occluding, the higher concentration of Ag#1
309 overcomes the occlusion disadvantage, albeit with a slow growth rate. The resulting MBC#1 population is

much closer to that of the bivalent cooperative case. However, although the greater abundance of Ag#1 amplifies the total BCR#1 response, it also reduces the competition for this Ag, which results in a lower overall affinity of the resulting B-cells (Fig. 7C).

For completeness, in SI Appendix S3 we repeated the above simulation while systematically varying the number of BCR/epitope pairs (2-15), occlusion parameter value (0,0.5,0.9,1), with three values of affinity advantage provided to the BCR#1, and with the BCR#1s bound monovalently or bivalently. The results are summarized in Fig. S7. In all cases, increasing Ag concentration leads to greater MBC output, with the increase being larger if the corresponding BCR also has a significant affinity advantage. The increased MBC output is associated with decreased affinity, however, and the affinity decrease is larger for monovalent than bivalent BCR#1s. The results therefore suggest that epitope subdominance can be overcome by increasing epitope concentration in vaccinations with cocktails of designed antigens, as proposed by others.(28, 29, 26) However, this is achieved at the expense of a reduction in the affinity of the resulting MBCs. For vaccine design, the precise Ag concentrations may need to be optimized to achieve a compromise between MBC population size and affinity for antigen.

We caution, however, that the above results should be considered qualitative, because our model does not incorporate a saturating Ag concentration, which could be done in fugure versions, *e.g.*, by explicitly modeling immune complexes or FDCs. Thus, the strong dependence of B-cell response on the Ag concentration is most likely relevant in a scenario where the total antigen amount is low.

Finally, to investigate whether the outcome of multiple vaccinations can be optimized by manipulating the epitope concentrations corresponding to monovalent BCRs, we simulated six consecutive immunizations under the same initial conditions as described before, except that the concentration of Ag#1 was increased in some, but not all, of the simulations. Specifically, we considered three immunization scenarios, in which the total nondimensional concentration of Ag#1, α_1^T=[Ag#1/Ag#i>1], in the six consecutive immunizations was (1, 1, 1, 1, 1, 1), (2, 1, 1, 2, 1, 1), and (2, 2, 1.5, 1.1, 1, 1). These three scenarios were chosen to determine whether increased Ag#1 occurring early in a vaccination regimen would translate into superior responses in later exposures. Figures 8 and S8 show the MBC output and affinity, respectively, at the end of each immunization for ten BCR/epitope pairs (other cases are omitted for clarity, but are qualitatively similar). Consistent with the previous results, MBC#1 output after a particular immunization increases if Ag#1 used in that immunization is increased (and vice versa), and the MBC#1 affinity decreases if Ag#1 used in that immunization is increased (and vice versa). However, the differences between the three protocols essentially disappear after the final exposure, hence the present model suggests that there may not be a significant long term immunological effect of simply manipulating antigen concentration in a vaccine.

We also note that, in the idealized case of a uniform antigen concentration profile, the normalized BCR affinities for antigen rise uniformly to a plateau around the 5th exposure (Fig. S8). However, the results show a sensitivity to the antigen concentration profile, suggesting that the number of exposures needed to elicit high-affinity antibodies generally depends on the details of the exposure, such as epitope concentration, or whether the exposure is by vaccination or natural infection.

3 DISCUSSION

Rapidly mutating and proliferating viruses such as influenza, HIV, and, more recently, SARS-CoV-2, accumulate escape mutations that can render existing host immunity obsolete. However, because such
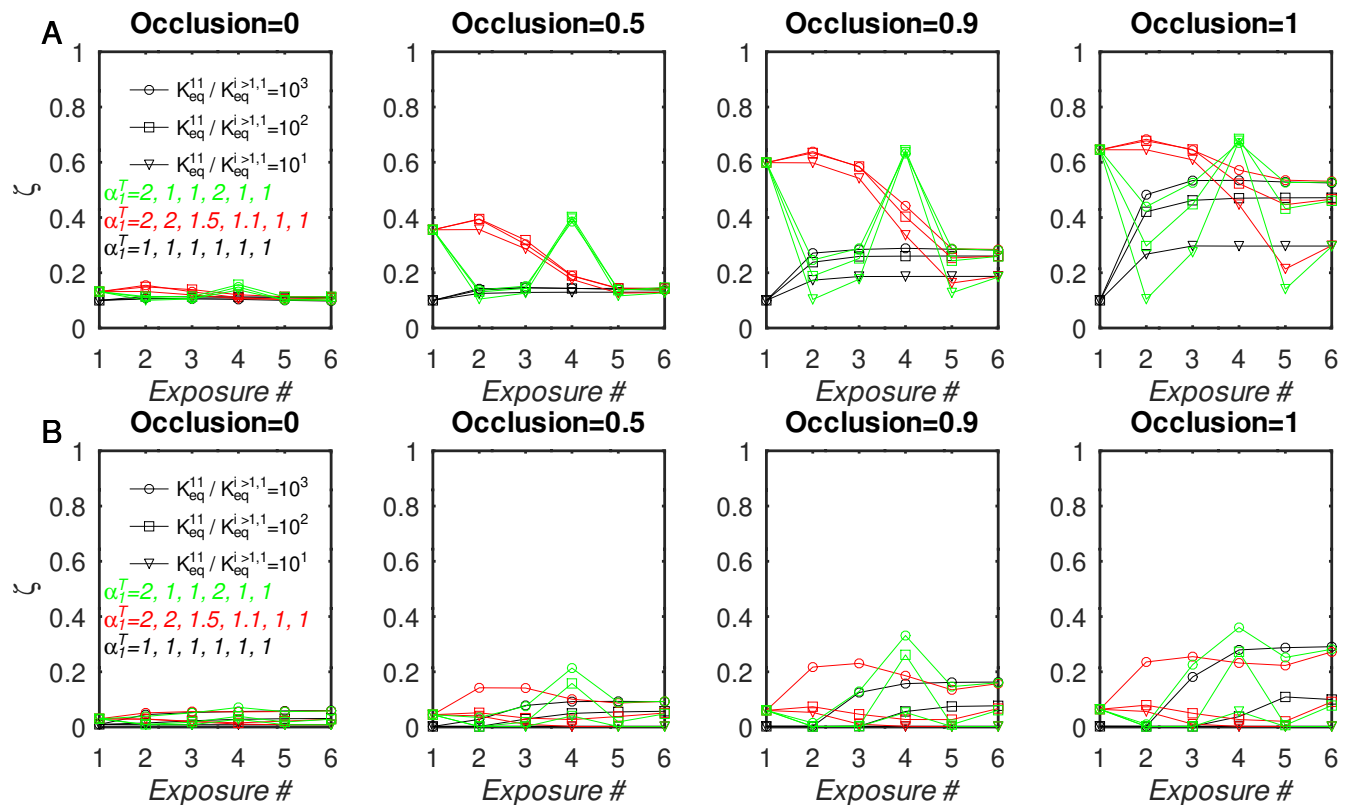
Figure 8. Fraction of MBC#1 *vs.* number of sequential GC simulations for different initial affinity advantage values and different Ag#1 concentrations, with 10 total BCR/Epitope pairs. A & B: MBC#1 fraction (ζ) at the end of simulations. A: BCR#1 is cooperatively bivalent ($K_{eq}^{12}=10K_{eq}^{11}$); B: BCR#1 is monovalent ($K_{eq}^{12}=0$). The four sets of panels A and B show the effect of increasing occlusion from $o=0$ (no competition) to $o=1$ (full competition).

351 pathogens must maintain infectivity to survive, some mutations are highly improbable, as they would
352 significantly reduce or even eliminate viral fitness. In addition, selection pressure from the immune system
353 is variable along the antigenic sequence (*e.g.* solvent-exposed regions are more susceptible to antibodies
354 than buried ones). The resulting differences in mutation propensities make it possible to partition the viral
355 topology into variable and conserved epitopes. Unfortunately, variable epitopes tend to be immunodominant,
356 *i.e.* they are the main targets of adaptive immunity. Immunodominance, in itself, may be the result of
357 viral adaptation; for example, the large highly-variable head of influenza hemagglutinins is an entropic
358 distraction to the immune system. A major focus of current vaccine research is to elicit a potent and durable
359 immunity to conserved, immunosubdominant, epitopes. Such vaccines would lower HIV infection rates, or
360 eliminate the need for a yearly influenza vaccine.

361   Here, we employed a coarse-grained model of affinity maturation (AM) parametrized using experimental
362 data on germinal centers (GCs)(42, 44, 43) to determine whether differences in B-cell receptor (BCR)
363 binding valency could explain the subdominance of certain epitopes. The main assumption of the model
364 is that B-cell activation increases with the amount of equilibrium-bound BCR to antigen (Ag). More
365 specifically, when both arms (Fabs) of BCR bind the antigen displayed on follicular dendritic cells
366 (FDCs), the probability of internalizing the Ag increases, even if the affinity of each receptor for Ag is
367 weak. This assumption appears to be in accord with the experiments; Arevalo et al. (20) interpreted their
368 vaccination boosting data by suggesting that many weak BCR/Ag interactions are sufficient to activate

---

B-cells. Compelling indirect evidence comes from co-display of different Ags on nanoparticles, which was demonstrated to preferentially elicit broadly-neutralizing Abs. These findings(28, 29) imply that avid bivalent binding confers a proliferation advantage, which is consistent with the present model. However, as B-cell activation by Ags is a complicated process, involving cross-linking of the BCRs, it is not clear to what extent avid binding would increase crosslinking. Future experiments and simulations may be needed to shed more light on the activation process.

The present simulations indicate that monovalent B-cells always grow more slowly than bivalent ones, and are therefore easily dominated by B cells that are able to bind bivalently and cooperatively. When given an initial affinity advantage over bivalent B-cells, as might be expected to occur upon recruitment of monovalent memory cells (MBCs) into secondary GCs, the affinity advantage was often insufficient to overcome the slower growth. The monovalent B cells outcompeted bivalent ones only if the affinity advantage was more than an order of magnitude (see Fig. 6B). These results are in agreement with influenza vaccination experiments, which show that a boost with a pandemic strain for which the host has little immunity against epitopes in the HA head, produces high anti-HA stem titers; a subsequent boost with the same vaccine elicits anti-HA head Abs.(18) We have interpreted these experimental data by assuming that anti-HA stem Abs bind monovalently with a high affinity advantage in the first vaccination, but not the second. In the second vaccination, the bivalent anti-HA head Abs are able to overcome the advantage *via* maturation induced by the first shot.

Rather than relying solely on an affinity advantage, a more robust method to boost monovalent B-cells is to increase the concentration of their cognate epitope(s). The simulations indicate that this approach results in the highest number of monovalent MBCs (see Figs. 7 and 8 in Sec. 2). The finding is not surprising, since the presence of foreign antigen is what initiates and sustains GC reactions in the first place. However, because selection among B-cells is driven by competition for Ag, an increase in available Ag will allow lower-affinity BCRs to survive. Thus, although the corresponding monovalent Abs become more numerous with increased epitope concentration, they evolve lower average affinity. When we simulated a subsequent GC reaction initialized with MBCs from such a memory pool, but *without* the concentration advantage (designated by $\alpha_1^T = 1$ in the results), as would occur in a natural infection, the monovalent B-cell population rapidly decreased, such that after two such consecutive GC reactions, there was no difference when compared to vaccinations in which the concentration of the Ag cognate to the monovalent Ab was never increased (Fig. 8).

These results suggest that increasing Ag concentration might only provide a temporary advantage to the cognate BCRs, as Ag levels are easy to manipulate in vaccination, but not in infection. Nevertheless, the strategy could prove useful to expand the number of initial low-affinity B-cell lineages targeting rare epitopes against which high-quality B-cell precursors are rare, such as group I and II influenza stem epitopes, as also suggested in a recent computational study of COVID vaccine efficacy.(54)

If subsequent exposures *via* natural infection restore immunosubdominance,(18) regular vaccine boosting with higher concentrations of subdominant epitopes could be required.

We note that multi-antigen vaccination cocktails have been designed, in which the epitopes that are conserved between the antigens are at effectively higher concentration than variable epitopes.(28, 29, 26) In particular, mosaic nanoparticles appear to elicit a broader antibody response in animal experiments, compared to cocktail immunizations.(28, 29) However, it remains to be shown whether such vaccines will lead to improved protection against highly mutable pathogens in the clinic. Simulations performed here suggest that such cocktails have promise to elicit

412 Abs to conserved epitopes *via* a concentration advantage. Future experiments are needed to address whether
413 the resulting immunity would persist after multiple rounds of natural infections.

414 The model used here relies on simple assumptions to show that for different epitopes
415 with similar accessibilities, which can be interpreted as similar effective concentrations,
416 immunosubdominance can be explained by differences in the antibody binding valency. This
417 scenario appears applicable to the case of natural immunity against influenza hemagglutinins,
418 as Harris et al. (27) have shown that most of the trimeric HA spikes are able to bind an anti-
419 stem antibody. The arrangement of the spikes makes it likely that bivalent binding would be
420 disfavored by energetic strain.(27, 24) A related scanario applies in the case of HIV, in which
421 low spike density makes bivalent binding unlikely, but antibodies engineered with long linkers
422 that could bind the same trimeric spike bivalently exhibited > 100-fold greated potency.(55)
423 However, binding valency alone cannot adequately explain immunodominance that arises in
424 vaccination using soluble HA ectodomains, because head and stem epitopes would be expected
425 to have similar antibody accessibilities. Therefore, other factors, such as antigen plasticity, low
426 natural germline precursor frequency, repertoire filtering due to self-reactivity, or reduced T-cell
427 help,(41) must also contribute. For example, Keating et al. (56) employed several methods of
428 partially inhibiting GC formation in mice, and showed that the proportion of bnAbs in GC-inhibited
429 mice was not increased relative to wild-type mice or untreated mice. The findings were used
430 to argue that the predominant reason for low bnAb prevalence was not competition between
431 antibody lineages, but other factors, such as removal of bnAb precursors due to immune tolerance
432 mechanisms.(56) Such factors could also explain why antibodies produced in natural infections
433 such as SARS-Cov-2 tend to target relatively few antigenic epitopes, despite high overall antigen
434 accessibility.(57)

435 Some of the aforementioned factors could be incorporated into the model in an approximate way in
436 future studies. The effects of adjuvants on B-cell activation can be modeled by parametrizing the
437 B-cell activation function to include adjuvant concentration, or by incorporating the latter into
438 a T helper cell model. Similar ideas could be used to include the effects of soluble signaling
439 species, such as interleukins or Calcium ions. Further, more sophisticated approaches that
440 explicitly model BCR evolution in sequence space and/or compute BCR/Ag binding affinity using
441 structural models have been developed. For example, Robert et al. (58) approximated B-cell and
442 Antigen interactions by discretizing the epitope and paratope on a lattice, and using an empirical
443 inter-residue potential.(58) The authors were able to capture key properties of multi-antigen
444 vaccinations, such as increased cross-reactivity in cocktail immunizations. However, BCR/Ag
445 models at all-atom resolution,(59, 60) which may be parametrized to account for antigen stability
446 and rigidity, may ultimately be required to design actual vaccine antigens and their cocktails.

447 For the practical purpose of universal vaccine design, we can summarize the interpretation of
448 our simulation results as follows. HA stem epitopes presented on influenza virions are immuno-
449 subdominant due to an inability to recruit bivalently-binding BCRs, combined other causes
450 of subdominance. Even if vaccination with soluble antigen ectodomains elicited an anti-stem
451 response, it would not be boosted in secondary GCs formed upon subsequent natural reinfection,
452 because the corresponding B-cells would be unable to bind antigen bivalently. It remains to be
453 shown whether this disadvantage could be overcome by devising vaccines that present stem
454 epitopes for bivalent binding, *e.g.* by using engineered immunogens attached to nanoparticles,(52)

possibly in a mosaic arrangement(29), or by immunizing with cocktails with very similar stems but diverse heads(26).

While immunization with diverse coronavirus receptor binding domains presented as mosaic nanoparticles elicited a broad antibody response, including to strains not present in the vaccine,(29) when this strategy was applied to a diverse panel of influenza HA spikes, the resulting breadth was no greater than that observed with immunizations using homotypic nanoparticle cocktails.(61) The interpretation was that the epitopes in the mosaic panel were too dissimilar to allow significant bivalent binding, which suggests that careful tuning of antigen sequence similarity may be needed to elicit broad responses *via* a concentration advantage.

4   METHODS

Model of Germinal Center Affinity Maturation

The model of affinity maturation (AM) used here is based on the work of Kepler and Perelson (32), who used systems of coupled differential equations to calculate the concentrations of B-cells of different discrete affinities for an antigen (Ag). We have generalized the model to simulate the maturation of multiple B-cell lineages, each binding to its cognate antigen mono- or bivalently, and producing memory B-cells and plasma cells, which secrete antibodies of the same affinity for the cognate Ag. The model does not have any geometric or topological component to represent binding, and, where there is no ambiguity, we sometimes use the terms antigen and epitope interchangeably. We will also sometimes use the abbreviation BCR (B-cell receptor) to refer to B-cells, with the implicit scaling assumption that each B-cell has $\sim 10^5$ BCRs on its surface.(62, 63)

We assume that the simulated germinal center(s) (GCs) have been seeded by N_B B-cell lineages B^i, and that each lineage can bind only to its cognate antigen a_i. Though the model is based on the system of differential equations of Kepler and Perelson (32), it has several important additions, notably memory cell, plasma cell, and antibody production. For clarity, we first present a minimal version of the model, which is close to the original B-cell model(32) and describe the modifications in subsequent subsections.

4.0.1   Basic model

For each B-cell lineage, we explicitly model its binding affinity distribution. Specifically, we assume that (1) the equilibrium binding affinity K_{eq}^i of any B-cell B^i derived from the lineage i for its cognate antigen a_i is in the range $K_{eq}^{min} \leq K_{eq}^i \leq K_{eq}^{max}$ and (2) that the affinities can be represented by a discrete set of values, as follows. We assign to each B^i a binding energy index $j \geq 1$ such that

$$\log K_{eq}^{min} \leq (j-1)\Delta E + \log K_{eq}^{min} \leq \log K_{eq}^i < j\Delta E + \log K_{eq}^{min} \leq \log K_{eq}^{max} + \Delta E. \qquad (1)$$

Equation (1) corresponds to a uniform discretization of binding affinities in logarithmic space with energy grid spacing ΔE, or exponential discretization in affinity space.

As done by Kepler and Perelson (32), we will refer to the energy bins j as *affinity classes*. Their number, N_ϵ, is related to ΔE by $\log K_{eq}^{max} - \log K_{eq}^{min} = (N_\epsilon - 1)\Delta E$. We take N_ϵ=20 (see Table 1), which implicitly determines ΔE once K_{eq}^{min} and K_{eq}^{max} are chosen. In the simulations, we only allow values of K_{eq} that correspond to the bin edges, *i.e.*, $K_j^i = K_{eq}^{min} e^{(j-1)\Delta E}$, $1 \leq j \leq N_\epsilon$, where, for brevity, we replaced the subscript eq by the affinity class index j.

491   To simulate affinity maturation, we compute the time evolution of B-cell populations in each affinity
492   class j using

$$\frac{d[B_j^i]}{dt} = \left\{-k_d(1 - h_j^i) - k_p\right\}[B_j^i] + 2k_p \sum_{k=1}^{N_\epsilon} m_{kj}[B_k^i],$$

$$\text{for } 1 \leq i \leq N_B,$$

(2)

493   where k_p and k_d are proliferation and death constants, respectively, m_{kj} is the probability for a BCR B^i in
494   affinity class k to transition to affinity class j *via* somatic mutations that take place during AM, h_j^i is B-cell
495   activation function (discussed below), and N_B is the number of different B-cell lineages.
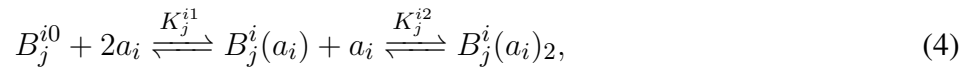
496   The class transition probabilities m_{jk} are assumed to be independent of the lineage i, and are defined as

$$m_{jk} = \frac{[\mu(1 - p_L)]^{|k-j|}}{|k-j|!} \frac{\exp(-\mu)}{1 + \Lambda^{2(k-j)}}, \quad j \neq k$$

$$m_{jj} = 1 - \sum_{k \neq j}^{N_\epsilon} m_{jk},$$

(3)

497   where Λ determines the ratio of advantageous to non-lethal deleterious mutations, p_L is the probability
498   of lethal mutations, and μ is the probability of an expressed (*i.e.* nonsilent) mutation per generation.(32)
499   Kepler and Perelson (32) used an oscillating function for $\mu(t)$ to mimic the effect of interconversion of
500   centroblasts and centrocytes on the mutation rate, which was optimized to maximize a 'total' affinity $A(t)$
501   of mature B-cells of a single lineage $i{=}1$ ($A(t) = \sum_j^{N_\epsilon}[B_j^1]K_j^1$). We use a constant average mutation rate
502    $\mu{=}0.1$, which is appropriate for comparing growth rates of different BCR lineages within the framework of
503   this coarse-grained model; otherwise one would need to specify the phases of oscillation for each lineage,
504   which are unknown, and might furthermore be stochastic. The constant value $\mu{=}0.1$ was also used by
505   Oprea and Perelson (33).

506   The activation function h_j^i is derived from the proportion of the B cells, B_j^i, that receive a survival signal
507   *via* binding to antigen and/or helper T-cells (Tfh). In the simpler model, which involves only activation by
508   antigen (Ag), h_j^i is computed from the equilibrium fraction of receptors B_j^i bound to the cognate Ag a_i.
509   Because each BCR has two binding arms (Fabs), we assume the binding reactions

$$B_j^{i0} + 2a_i \underset{}{\overset{K_j^{i1}}{\rightleftharpoons}} B_j^i(a_i) + a_i \underset{}{\overset{K_j^{i2}}{\rightleftharpoons}} B_j^i(a_i)_2,$$

(4)

510   corresponding to sequential binding of the first and second Ags to free B-cells (B_j^{i0}). From the conservation
511   of total B cells B_j^i,

$$[B_j^{i0}] + [B_j^i(a_i)] + [B_j^i(a_i)_2] = [B_j^i],$$

(5)

512   we have

$$[B_j^i(a_i)] = \frac{K_j^{i1}[B_j^i][a_i]}{1 + K_j^{i1}[a_i](1 + K_j^{i2}[a_i])}$$

(6)

513   and

$$[B_j^i(a_i)_2] = \frac{K_j^{i1}K_j^{i2}[a_i]^2}{1 + K_j^{i1}[a_i](1 + K_j^{i2}[a_i])},$$

(7)

514 which allows us to compute the fraction of bound BCR arms (two per BCR), provided that the concentration
515 of free Ag, $[a_i]$, is known, *i.e.*

$$\theta_j^i = \frac{[B_j^i(a_i)] + 2[B_j^i(a_i)_2]}{2[B_j^i]}. \tag{8}$$

516 In the above, K_j^{i1} and K_j^{i2} are equilibrium binding constants, corresponding to binding by a first BCR arm
517 and the second, respectively. K_j^{i1} is equal to the affinity of the Fab, *i.e.*, $K_j^{i1}=K_j^i$, and K_j^{i2} is taken to be
518 proportional to it, $K_j^{i2}=C_i K_j^i$, where the constant C_i is affinity-independent, and reflects geometry-related
519 factors that influence the binding of the second arm, such as excluded volume (entropy), and deformation
520 strain (energy) required to position the second arm for binding. Monovalent binding corresponds to $C_i = 0$.
521 Other values of C_i used in the simulations were 1 and 10, which are discussed in the next subsection.

522   To evaluate Eqs. (6) and (7), $[a_i]$ is needed. Writing conservation of total antigen $[a_i^T]$, which is prescribed
523 at the beginning of the GC reaction, and possibly evolves during the reaction, we have

$$[a_i] + 2\sum_{j=1}^{N_\epsilon}[B_j^i]\theta_j^i = [a_i^T]. \tag{9}$$

524 We solve Eq. (9) for $[a_i]$ iteratively using the Newton-Raphson method.(64)

525   With θ_j^i determined, we can compute the activation h_j^i. Kepler and Perelson (32) modeled a single lineage
526 and used $h_j^1=2\theta_j^1$ with $K_j^{12}=0$, *i.e.*, they treated all BCRs as monovalent. In the present model, we modified
527 the functional form of h to match the observations of GC size evolution of Wittenbrink et al. (42), while
528 keeping most of the parameters from the KP93 model(32). Specifically, we defined the activation function
529 as

$$h_j^i = \rho(\theta_j^i)^\epsilon \tag{10}$$

530 and performed least squares optimization to improve agreement with the average GC data(42), to obtain
531 ρ=0.94 and ϵ=0.7 (see SI Appendix S4 & Fig. S9). Because $\theta_j^i < 1$, the prefactor reduces the activation
532 upper bound to ρ; the exponent $\epsilon < 1$ increases activation for smaller binding fraction values, reducing the
533 competitive advantage of higher affinity BCRs.

534   Two comments on Eq. (2) are necessary. First, the proliferation is split into two terms(32) to expose the
535 fact that mutations in a cell of lineage B_j^i during division will lead to the loss of the parent cell and a gain of
536 two daughter cells. Second, the proliferation is not *activated* (*i.e.* not proportional to h_j^i). Whether activation
537 by Ag and T-cells mainly rescues B-cells from apoptosis (death rate proportional to [1-h]),(65, 36) or
538 actually increases the rates of proliferation (growth rate proportional to h) has been a matter of some debate,
539 with more recent evidence in favor of activated proliferation.(66) In this study, however, parametrizing
540 the model with activated proliferation would not change the main conclusions; the main difference in the
541 activated proliferation model parameters was that the rate constants k_p^{max} and k_d had to be increased and
542 reduced, respectively, to fit experimental data (see SI Appendix S5). The fact that in the *nonactivated*
543 proliferation model the B-cell death rate constant is higher than the proliferation rate (Table 1) reflects
544 the importance of rescue from apoptosis to B-cell survival for this model. Comparison of the activated
545 proliferation model results to the experiments(42, 44) is given in Figs. S10 and S11. A study of the two
546 types of proliferation models was performed by Amitai et al. (67), whose main finding was that activated
547 proliferation reduces clonal diversity.

548 4.0.2 Avidity of simulated BCRs

549 To examine the effect of BCR avidity on the evolution of B cells within the GC, we compare the behavior
550 of lineages with three regimes of bivalency, corresponding to K_{eq}^2=0, K_{eq}^2=K_{eq}^1, and K_{eq}^2=10K_{eq}^1, which we
551 denote, respectively, as the monovalent, noncooperative, and cooperative binding cases. We can rationalize
552 the chosen values as follows. The binding constant can be expressed in terms of the free energy difference
553 (ΔF) between reactants and products, which is approximately decomposable into rotational, translational
554 (equivalently, concentration) and configurational components(68); Because the two binding arms (Fabs)
555 are identical, we assume that they populate identical conformational ensembles, and therefore their ΔF
556 of binding can only differ in the rotational and translational entropies, and, possibly, in the energetic
557 strain needed to move the second Fab into its binding position. The translational entropy penalty of
558 binding of the second Fab (Fab2) will generally be much smaller than that of the first (Fab1), because
559 the volume accessible to unbound Fab2 is restricted by the binding of Fab1 to its epitope, whereas the
560 volume accessible to an unbound BCR is of the order of the GC volume. More specifically, we can estimate
561 the volume available to Fab2 when Fab1 is bound to be the volume occupied by an antibody, which is of
562 the order $(10nm)^3 = 10^{-24}m^3$. The effective AG concentration is inversely proportional to this volume
563 (*i.e.* we assume that one antigenic site is available to Fab2, restrained by Fab1). In contrast, when Fab1
564 is unbound, we take the AG concentration to be inversely proportional to the volume of the GC light
565 zone, approximated as 50% of the GC volume ($= 0.5 \times [80\mu m]^3 = 2.56 \times 10^{-13}m^3$) and proportional
566 to the number of individual Ags presented on FDCs. Because antigen is generally abundant in GCs,(69)
567 we take the number of Ags available to bind BCRs as 1000 times the typical B-cell count in a maturing
568 GC, which is around 2000 from Fig. 3. The ratio of antigen concentrations for bound *vs.* unbound Fab1
569 is then $10^{24} \times 2.56 \times 10^{-13}/(1000 \times 2000) \simeq 10^5$. The difference in the rotational entropy penalty due
570 to binding is expected to be much smaller, because antibodies appear to be sufficiently flexible to permit
571 considerable independent rotation of the individual Fabs.(70) In particular, we expect the difference to be
572 less than an order of magnitude, and neglect this contribution. If energetic strain (*i.e.* ΔE) is needed to
573 accommodate binding of Fab2, it will reduce the binding affinity by the factor $\exp(\Delta E/[k_B T])$. In the
574 absence of experimental data, we assume a strain energy in the range 1-5 kcal/mol, which corresponds to
575 the reduction of K_{eq}^2 by a factor in the range $\exp(1/[k_B T]) - \exp(5/[k_B T]) \simeq 5$–4160, where $k_B T \simeq 0.6$
576 at T=300K. The above crude estimates suggest that, even with a substantial antibody strain of 5kcal/mol, a
577 bivalency binding advantage of $\times 25$ would be present. For simplicity, and to include a margin of safety in
578 our results, we assume a slightly lower binding advantage factor of 10, *i.e.* K_{eq}^2=10K_{eq}^1. We also include
579 the monovalent case, $K_{eq}^2 = 0$, which can also be interpreted as requiring infinite strain energy for Fab2
580 binding, and an intermediate case K_{eq}^2=K_{eq}^1, which we label noncooperative.

581 A possibility that is beyond the scope of this work is to compute strain energy from molecular dynamics
582 simulations of bivalent Ab/Ag binding. However, such simulations are expected to be difficult because of
583 the large sizes of the antibody and antigen molecules involved.

584 4.0.3 Memory cell production

585 The basic AM model, Eq. (2), follows the populations of B-cell lineages (i) with different affinities (j).
586 However, we are also interested in the memory B-cell (MBC) populations produced by different lineages,
587 since these MBCs will be activated in the host upon repeat infections. As in our earlier modeling work,(17)
588 we assume that some of the B-cells exit the GC reaction as MBCs or plasma cells (PCs). MBCs are
589 discussed here and PCs, in the next subsection.

590   Using M_j^i to denote MBCs of lineage i and affinity j, the corresponding evolution equation is

$$\frac{d[M_j^i]}{dt} = C_M h_j^i (1 - h_j^i)[B_j^i] - k_d^M[M_j^i], \tag{11}$$

591   where the first term corresponds to differentiation from GC B-cells, and the second, to apoptosis. The
592   fraction $h_j^i(1 - h_j^i)$ preferentially selects B-cells of intermediate affinity, reflecting the observation that
593   higher-affinity B-cells are more likely to recycle into the dark zone, rather than exit as MBCs.(71) The
594   value of C_M is 0.3 (discussed further later) and the death rate constant k_d^M is 0.02/day(72).

595   ### 4.0.4   Plasma cell and antibody production

596   Under the assumption of constant Ag concentration, Eqs. (2) converge to a steady-state solution, in
597   which the GC is composed of highest-affinity B-cells, surviving indefinitely.(32) However, it is known
598   that GCs shrink to 5% of their maximum size after about a month.(73) While the assumption of constant
599   antigen used in Ref. 32 is likely to be unrealistic, Ag consumption in the GC is not the main cause of GC
600   shrinkage. It is known that immune complexes presented by follicular dentritic (and other) cells(39) persist
601   for very long times, which is probably necessary for immune memory maintenance.(74)

602   To account for Ag consumption, we follow Rundell et al. (72) and model it by exponential decay,

$$\frac{d[a_i^T]}{dt} = -k_d^a[a_i^T], \tag{12}$$

603   with k_d^a=0.011/day, which corresponds to a half life of about 63 days.

604   To model GC shrinkage consistently with the experimental observations of GC size,(42) we adopt the
605   antibody feedback model of Zhang et al. (31). The essential concept is that some of the maturing B-cells
606   differentiate into PCs, which secrete Abs. These Abs can diffuse throughout the GCs and compete with
607   BCRs for antigen. Once the Abs are sufficiently numerous and of high affinity, the GC shrinks. Although
608   the process of GC shrinkage is probably considerably more complicated, involving regulatory T cells and
609   various signaling molecules, we employ the Ab feedback model here because it requires few additional
610   variables and parameters (see below), and is able to capture GC size evolution over time, as shown here
611   and in Ref. 31.

612   Since antibodies are secreted by PCs, we began with the PC evolution equation

$$\frac{d[P_j^i]}{dt} = C_P h_j^i (1 - h_j^i)[B_j^i] - k_d^P[P_j^i]. \tag{13}$$

613   However, our attempts at fitting this model to the PC production data of Weisel et al. (44) did not yield
614   good agreement. The main reason is that the MBC and PC production rates have different evolution
615   profiles in the experiments (see Fig. 3B *vs.* Fig. 3C), with the MBC rate decreasing rapidly, while the
616   PC rate remains essentially constant within the experimental uncertainty. In contrast, our models for the
617   two quantities (Eqs. (11) and (13)) are the same, except for the numerical values of the parameters. To
618   improve agreement in the PC rate, we added an additional, semiempirical, source term to Eq. (13), $k_M^P[M_j^i]$,
619   to mimic low-level differentiation of MBCs activated by immune complexes carrying antigen into late

620   B-blasts, which differentiate into long-lived PCs.(75, 72) The resulting PC evolution equation is

$$\frac{d[P_j^i]}{dt} = C_P h_j^i (1 - h_j^i)[B_j^i] + k_M^P[M_j^i] - k_d^P[P_j^i], \tag{14}$$

621   which maintains some PC production even if the B-cell (but not MBC) population vanishes.

622   In Eq. (14) the value of the death rate constant k_d^P is 0.0336/day(72), the differentiation constant C_P is 0.7,
623   and the production constant k_M^P is 0.18/day. C_P and k_M^P were first set by trial and error and subsequently
624   refined by least squares fitting to reproduce the average GC dynamics. While we could not obtain a
625   biologically-motivated value for k_M^P, we note that it is about an order of magnitude lower than the B-cell
626   proliferation constant (see Table 1), consistent with its role as a lesser source of PCs. However, its value
627   still appears to be unphysically high, especially in comparison to the MBC death rate of 0.02/d (Eq. (11)),
628   possibly reflecting deficiencies or oversimplifications in the differentiation components of the model. For
629   example, the probabilities of a B-cell exiting the GC to differentiate into an MBC *vs.* a PC are kept constant
630   (C_M=0.3 *vs.* C_P=0.7). Recent data suggests that PCs tend to be produced more frequently in later stages of
631   the GC reaction,(44) and that a PC is more likely to result than an MBC if the B-cell has higher affinity for
632   antigen, and/or receives more T-cell help.(71) However, because quantitative data describing the relative
633   MBC/PC output is scarce and imprecise, we do not implement an affinity dependence in the MBC/PC
634   differentiation choice, and instead use the same preference for B-cells of intermediate affinity in both cases
635   *via* the factor $h_j^i(1 - h_j^i)$ in Eqs. (11) and (14). More sophisticated affinity-based cell fate decisions are
636   probably needed in these equations. They can be modeled using other functions of h_j^i, or by introducing
637   other biological species or signaling molecules, as more precise data become available.

638   Antibodies are secreted by PCs and and their removal is modeled with exponential decay

$$\frac{d[A_j^i]}{dt} = k_p^A[P_j^i] - k_d^A[A_j^i]. \tag{15}$$

639   The Ab death rate constant k_d^A is obtained from the half-life of 10d,(31) and an approximate secretion k_p^A
640   rate constant is obtained as follows. We assume that every PC secretes 1.7×10^8 Ab molecules/day(76).
641   However, the Abs are allowed to diffuse freely in and out of GCs, and, assuming that the diffusion
642   is fast enough to establish equilibrium, we scale this rate by the ratio of internal to external volumes
643   corresponding to a single GC. The internal volume is taken as the volume of a sphere of radius $80 \mu m$,(42)
644   and the external volume is taken to be $0.04mL$(31), which gives k_p^A=8500/day. Starting from this value, and
645   the PC differentiation parameter C_P=0.5, we used least squares fitting to improve the agreement between
646   the model and the average GC sizes of Wittenbrink et al. (42) (an example of parameter fitting is shown in
647   SI Appendix S4). The optimized values were k_p^A=35000/day and C_P=0.7, corresponding to higher values
648   of Ab production needed to achieve faster GC shrinkage.

649   The effect of Ab competition is incorporated by modifying the Ag conservation Eq. (9) to include binding
650   to Abs,

$$[a_i] + 2\sum_{j=1}^{N_\epsilon}([A_j^i/\sigma] + [B_j^i])\theta_j^i =$$

$$[a_i] + \sum_{j=1}^{N_\epsilon}[C_j^i]\theta_j^i = [a_i^T], \tag{16}$$

651 where we assumed that Abs bind antigen in the same manner as do BCRs, and defined a total receptor
652 concentration $[C_j^i] \equiv 2([A_j^i/\sigma] + [B_j^i])$; the scaling factor $\sigma = 10^5$ appears because each B-cell (B_j^i) is
653 assumed to have 10^5 BCRs,(62) which have the same binding valency as Abs.

654   At this stage, the model, as written in Eq. (2), does not have explicit limitations on the maximum GC size.
655 The shape of the B-cell population curve is governed entirely by proliferation, death and competition with
656 Abs. To obtain a close match to the peak in the experimental B-cell count,(42) we follow others (33, 72)
657 and introduce a maximum lineage size $B_{max} = 5000$ cells. The proliferation rate is modified as follows,

$$k_p = k_p^{max} \times \left(1 - \frac{\sum_j [B_j]}{B_{max}} \right), \tag{17}$$

658 where k_p^{max} is the maximum proliferation rate. A similar idea was used by Amitai et al. (24), who increased
659 the cell death rate, as a critical B-cell population was approached.

4.0.5 Clonal competition via epitope occlusion

661   Thus far, we have described a model which has competition only within each clonal lineage, *i.e.*, higher-
662 affinity cells outcompete lower-affinity cells, and are themselves eventually outcompeted by growing
663 numbers of high-affinity Abs derived from them. However, GCs are seeded by multiple lineages, and it is
664 therefore important to consider the effects of interclonal competition. In the context of influenza, it would
665 be of interest to model how anti-HA-head Abs could directly compete with anti-HA-stem Abs.

666   Toward this end, we generalize the model by introducing a distinction between epitopes and antigens.
667 Specifically, we recognize that a single antigen can present different epitopes. For example, an entire viral
668 spike may be considered an antigen with many different epitopes, each targeted by a different activated
669 B cell. We postulate that the binding of a BCR or Ab of type k to its cognate epitope a_k can reduce the
670 accessibility of epitope a_i, so that the effective concentration of a_i available to bind is reduced by a fraction
671 of the bound concentration of a_k. We label this reduction $\Delta^k[a_i]$, which is

$$\Delta^k[a_i] = -O_{ik} \sum_{j=1}^{N_\epsilon} [C_j^k]\theta_j^k, \quad \text{with } 0 \le O_{ik} \le 1, \ i \ne j, \tag{18}$$

672 where we introduced the *occlusion* tensor O_{ik}, which models the effect of epitope k occupancy on epitope
673 i. In particular, O_{ik}=0 corresponds to the absence of interaction, and O_{ik}=1 implies that binding of a_k
674 completely prevents binding to a_i (full occlusion). Setting $O_{ii} \equiv 1$, we write the modified Ag conservation
675 equations as

$$[a_i] + \sum_{j=1}^{N_\epsilon} \sum_{k=1}^{N_B} O_{ik}[C_j^k]\theta_j^k = [a_i^T], \tag{19}$$

676 in which the concentrations $[a_i]$ are now coupled *via* the occlusion tensor (unlike in Eq. (16), in which they
677 are independent). The components of O can in principle be set independently, provided that care is taken to
678 avoid component values so large that negative concentrations could result. For simplicity, we begin with a
679 constant occlusion independent of the antigen identity, *i.e.*, $O_{ik} = o$, for $0 \le o \le 1$, and $i \ne k$, and reduce
680 its value to prevent negative AG concentrations. Specifically, if $[a_k^T] > [a_i^T]$ we set

$$O_{ik} = o \times \min \left\{ 1, \frac{[a_i^T]}{[a_k^T]} \right\}. \tag{20}$$

681 In the simplified case of two BCR/epitope pairs, Eq. (20) can be justified as follows. We combine the
682 conservation equations,

$$[a_1] + \sum_{j=1}^{N_\epsilon}[C_j^1]\theta_j^1 + O_{12}[C_j^2]\theta_j^2 = [a_1^T],$$

$$[a_2] + \sum_{j=1}^{N_\epsilon}[C_j^2]\theta_j^2 + O_{21}[C_j^1]\theta_j^1 = [a_2^T] \tag{21}$$

683 to obtain

$$[a_1] + (1 - O_{12}O_{21})\sum_{j=1}^{N_\epsilon}[C_j^1]\theta_j^1 = [a_1^T] - O_{12}([a_2^T] - [a_2]). \tag{22}$$

684 Because $1 - O_{12}O_{21} \geq 0$ and the bound fraction θ^1 is zero only if $[a_1] = 0$ (we assume that the binding
685 constants are not both zero), to ensure $[a_1] \geq 0$, it is sufficient to require

$$[a_1^T] - O_{12}([a_2^T] - [a_2]) \geq 0, \tag{23}$$

686 or

$$O_{12} \leq \frac{[a_1^T]}{[a_2^T] - [a_2]}. \tag{24}$$

687 Eq. (20) satisfies this condition, since we also assume that $[a_2]$ is nonnegative.

688   We note that the occlusion tensor is similar in spirit to the interaction matrix used by Yan and
689 Wang (45). However, as these authors had a different purpose, specifically, to model synergistic
690 *vs.* antagonistic effects of Abs derived from previous B cell lineages on B cells in the current
691 generation, they allowed negative interference values, which are not physically justifiable in our
692 model, as they would imply creation of Ag.

4.0.6   Integration of model equations

694   In this section we describe the numerical procedures used to compute the time-dependent concentrations
695 of the Ags, cells, and Abs in the GC. First, following Kepler and Perelson (32), we make all concentrations
696 nondimensional using the total concentration of one of the antigens at the beginning of simulation.
697 For single-epitope (validation) simulations, we use the sole epitope. For multi-epitope simulations, we
698 aribitrarily elected to use the second epitope, to be able to vary the concentrations of the first epitope
699 for studying the effects of epitope concentration in maturation. Thus, the nondimensional variables are
700 $\alpha_i \equiv [a_i]/[a_2^T]$, $x_j^i \equiv [B_j^i]/[a_2^T]$, $y_j^i \equiv [A_j^i]/[a_2^T]$, $p_j^i \equiv [P_j^i]/[a_2^T]$, $w_j^i \equiv [M_j^i]/[a_2^T]$, and $\kappa_j^{ik} = K_j^{ik}[a_2^T]$.

In the new variables, the nondimensional evolution equations are

$$\frac{dx_j^i}{dt} = \left\{-k_d(1 - h_j^i) - k_p\right\} x_j^i + 2k_p \sum_{k=1}^{N_\epsilon} m_{kj} x_k^i, \tag{25}$$

$$\frac{dw_j^i}{dt} = C_M h_j^i (1 - h_j^i) x_j^i - k_d^M w_j^i, \tag{26}$$

$$\frac{dp_j^i}{dt} = C_P h_j^i (1 - h_j^i) x_j^i + k_M^P w_j^i - k_d^P x_j^i, \tag{27}$$

$$\frac{dy_j^i}{dt} = k_p^A p_j^i - k_d^A y_j^i, \tag{28}$$

$$\frac{d\alpha_i^T}{dt} = -k_d^a \alpha_i^T, \quad \text{for} \quad 1 \le i \le N_B,\ 1 \le j \le N_\epsilon. \tag{29}$$

and the nondimensional AG conservation equations are

$$\alpha_i + 2 \sum_{j=1}^{N_\epsilon} \sum_{k=1}^{N_B} O_{ik}(x_j^k + \sigma^{-1} y_j^k)\theta_j^k = \alpha_i^T, \tag{30}$$

$$\theta_j^i = \frac{1}{2} \cdot \frac{\kappa_j^{i1} x_j^i (1 + 2\kappa_j^{i2} x_j^i)}{1 + \kappa_j^{i1} x_j^i (1 + \kappa_j^{i2} x_j^i)}, \tag{31}$$

$$O_{ik} = o \times \min \left\{1, \frac{\alpha_i^T}{\alpha_k^T}\right\}, \tag{32}$$

701   and the expressions for m_{ij} and h are the unchanged.

702   We follow Kepler and Perelson (32) and take the dimensionless affinities $\kappa^{min} = 7.5^{-2}$, $\kappa^{max} = 7.5^5$,
703   but use N_ϵ=20 affinity bins, compared to their 8, for a finer discretization. This corresponds to $\Delta E \simeq 0.74$
704   in Eq. (1). Eq. (25) – Eq. (29) were integrated in Octave(77) using the explicit Euler method,(78) with the
705   time step $dt = 0.01 \times$day. At each iteration, Eq. (30) was solved for α_i using the iterative Newton-Raphson
706   (NR) method(64). The initial guess at the current iteration was taken as the corresponding value in the
707   previous iteration, which ensured that convergence required only a few NR iterations. At the beginning
708   of the simulation, the initial guesses were $\alpha_i = \alpha_i^T$. Simulation duration was 35 days, requiring less
709   than a minute of computer time using a single computing node with an Intel Xeon E5 2.3 GHz Haswell
710   CPU. However, the simulation cost was approximately linearly dependent on the number of BCR/Ag pairs
711   simulated. The simulation parameters and their values are listed in Table 1.

712   ### 4.0.7   Initial conditions

713   Initial values correspond to time t=0. For single-epitope simulations α_1^T=1. For multi-epitope simulations,
714   α_2^T=1, by definition of the normalization and α_i^T=1 for $i > 2$. The concentration of the first epitope
715   α_1^T was varied between 1 and 2, depending on simulation to investigate the effects of AG concentration
716   (see Results). The initial population of each B-cell lineage was 100 cells, because we assumed that a
717   mutation-free expansion of each seeding B-cell has already taken place prior to simulation. The initial
718   distribution of naive B-cell binding constants was log-normal; specifically, we used a Gaussian in the
719   energy space, centered on the 7th class ($\kappa \simeq 1.53$) with standard deviation σ=0.6 $\times$ Λ. This choice was

Table 1. Model and Simulation Parameters. Time is measured in days.

[†] Used only for computing cell counts *a posteriori*, *i.e.* does not impact simulations;

[‡] The affinity bounds apply only to the first binding constant κ_j^{i1}; the second binding constant was defined as different multiples of the first to investigate avidity effects (see Sec. 2);

[*] The ratio of advantageous to deleterious but nonlethal mutations is given by $1/(1 + \Lambda^2)$; It is computed by logarithmic scaling of the value Λ^0=30 of Kepler and Perelson (32) as $\log \Lambda = \Delta E \log \Lambda^0 / \log 7.5$, which accounts for the difference that Kepler and Perelson (32) used an 8-point disretization, or 8 affinity classes (corresponding to $\Delta E = \log 7.5$), while we use 20 classes.

Parameter	Description	Value	Source
k_p^{max}	maximum B-cell proliferation rate	2.2	adjusted from 4(Ref. 32) to fit data(42)
B_{max}	Maximum allowed B-cell count	5000	fit to data(42)
k_d	B-cell death rate	4.125	adjusted from 4(32) to fit data(42)
μ	BCR mutation rate	0.1	Oprea and Perelson (33)
σ	BCRs per B-cell	10^5	Casten and Pierce (62)
p_L	Fraction of lethal mutations	0.5	Kepler and Perelson (32)
C_M	MBC differentiation constant	0.3	fit to data(42, 44)
C_P	PC differentiation constant	0.7	fit to data(42, 44)
k_d^M	MBC death rate	0.02	Rundell et al. (72)
k_d^a	Decay of AG presented to BCRs	0.111	Rundell et al. (72)
k_d^P	PC death rate	0.0336	Rundell et al. (72)
k_M^P	PC production rate from MBCs	0.17	fit to data(44)
k_p^A	AB secretion from PCs	35000	based on Refs 76, 31 (see text)
k_d^A	AB death rate	0.069	Zhang et al. (31)
k_d^a	AG removal rate	0.011	Rundell et al. (72)
ρ	activation prefactor in $h = \rho\theta^\epsilon$	0.94	fit to data(42, 44)
ϵ	activation exponent in $h = \rho\theta^\epsilon$	0.7	fit to data(42, 44)
ξ	Concentration corresponding to one cell[†]	1e-4	Kepler and Perelson (32)
κ^{min}	Smallest (nondimensional) affinity[‡]	7.5^{-2}	Kepler and Perelson (32)
κ^{max}	Largest (nondimensional) affinity[‡]	7.5^5	Kepler and Perelson (32)
Λ	Mutation distribution constant[*]	$\simeq 3.5$	based on Ref. (32)
N_ϵ	Number of affinity classes	20	up from 8(Ref. 32) for higher resolution

720 made to approximate by a smooth function the discrete Dirac mass of κ=7.5, used by Kepler and Perelson
721 (32). The distribution is shown in Fig. 6D of the Results. The above distribution appears to us to be more
722 physical than the sharply peaked distribution of Kepler and Perelson (32). However, we note that we
723 could also obtain a satisfactory fit to the experimental data using the latter distribution, albeit with small
724 parameter adjustments that affect the total GC size and time to GC peak.

725   For simulations whose purpose was to investigate the effect of an initial affinity advantage on the rate of
726 B-cell proliferation (see Sec. 2), the initial distribution was shifted by scaling the abscissa by a prescribed
727 advantage (ΔK_{eq}), and linearly reinterpolated onto the initial grid in energy space (see Results and
728 Fig. 6D). All initial distributions (of each lineage) were normalized to 100 B-cells.

CONFLICT OF INTEREST STATEMENT

729 The authors declare that the research was conducted in the absence of any commercial or financial
730 relationships that could be construed as a potential conflict of interest.

AUTHOR CONTRIBUTIONS

VO conceived the research; VO performed the simulations; VO and MK analyzed results and wrote the paper.

FUNDING

ACKNOWLEDGMENTS

SUPPLEMENTAL DATA

Supplementary Material accompanies this article, including text appendices S1–S6 and figures S1–S13. The computer code to reproduce the simulation data and figures in this paper can be found online at `https://github.com/ovchinnv/affinity-maturation-paper2021.git`

REFERENCES

1 .Taubenberger J, Kash J, Morens D. the 1918 Influenza Pandemic: 100 Years of Questions Answered and Unanswered. *Sci. Trans. Med.* **11** (2019) 0. doi:10.1126/scitranslmed.aau5485.

2 .Andersen K, Rambaut A, Lipkin W, Holmes E, Garry R. the Proximal Origin of SARS-CoV-2. *Nat. Med.* **26** (2020) 450–452. doi:10.1038/s41591-020-0820-9.

3 .Bao Y, Bolotov P, Dernovoy D, Kiryutin B, Zaslavsky L, Tatusova T, et al. The Influenza Virus Resource at the National Center for Biotechnology Information. *J. Virol.* **82** (2008) 596–601. doi:10.1128/JVI.02005-07.

4 .MATLAB. *Version 7.10.0 (R2010a)* (Natick, Massachusetts: The MathWorks Inc.) (2010).

5 .Xu R, Ekiert D, Krause J, Hai R, Crowe J, Wilson I. Structural Basis of Preexisting Immunity to the 2009 H1N1 Pandemic Influenza Virus. *Science* **328** (2010) 357–60. doi:10.1126/science.1186430.

6 .Humphrey W, Dalke A, Schulten K. VMD - Visual Molecular Dynamics. *J. Mol. Graphics* **14** (1996) 33–38.

7 .Nachbagauer R, Choi A, Hirsh A, Margine I, Iida S, Barrera A, et al. Defining the Antibody Cross-Reactome Directed Against the Influenza Virus Surface Glycoproteins. *Nat. Immunol.* **18** (2017) 464–473. doi:10.1038/ni.3684.

8 .Corti D, Cameroni E, Guarino B, Kallewaard N, Zhu Q, Lanzavecchia A. Tackling Influenza with Broadly Neutralizing Antibodies. *Curr. Opin. Virol.* **24** (2017) 60–69. doi:10.1016/j.coviro.2017.03.002.

9 .Watanabe A, McCarthy K, Kuraoka M, Schmidt A, Adachi Y, Onodera T, et al. Antibodies to a Conserved Influenza Head Interface Epitope Protect by an IgG Subtype-Dependent Mechanism. *Cell* **177** (2019) 1124–1135.e16. doi:10.1016/j.cell.2019.03.048.

10 .Bajic G, Maron M, Adachi Y, Onodera T, McCarthy K, McGee C, et al. Influenza Antigen Engineering Focuses Immune Responses to a Subdominant but Broadly Protective Viral Epitope. *Cell host & microbe* **25** (2019) 827–835.e6. doi:10.1016/j.chom.2019.04.003.

11 .Raymond D, Bajic G, Ferdman J, Suphaphiphat P, Settembre E, Moody M, et al. Conserved Epitope on Influenza-Virus Hemagglutinin Head Defined by a Vaccine-Induced Antibody. *Proc. Natl. Acad. Sci. USA* **115** (2018) 168–173. doi:10.1073/pnas.1715471115.

12 .Bajic G, van der Poel C, Kuraoka M, Schmidt A, Carroll M, Kelsoe G, et al. Autoreactivity Profiles of Influenza Hemagglutinin Broadly Neutralizing antibodies. *Sci. Rep.* **9** (2019) 3492. doi:10.1038/s41598-019-40175-8.

13 .Kallewaard N, Corti D, Collins P, Neu U, McAuliffe J, Benjamin E, et al. Structure and Function Analysis of an Antibody Recognizing All Influenza a Subtypes. *Cell* **166** (2016) 596–608. doi:10.1016/j.cell.2016.05.073.

14 .Corti D, Voss J, Gamblin S, Codoni G, Macagno A, Jarrossay D, et al. a Neutralizing Antibody Selected from Plasma Cells That Binds to Group 1 and Group 2 Influenza a Hemagglutinins. *Science (New York, N.Y.)* **333** (2011) 850–6. doi:10.1126/science.1205669.

15 .Li G, Chiu C, Wrammert J, McCausland M, Andrews S, Zheng N, et al. Pandemic H1N1 Influenza Vaccine Induces a Recall Response in Humans That Favors Broadly Cross-Reactive Memory B Cells. *Proc. Natl. Acad. Sci. USA* **109** (2012) 9047–52. doi:10.1073/pnas.1118979109.

16 .Prigent J, Jarossay A, Planchais C, Eden C, Dufloo J, Kök A, et al. Conformational plasticity in broadly neutralizing hiv-1 antibodies triggers polyreactivity. *Cell Rep.* **23** (2018) 2568–2581. doi:10.1016/j.celrep.2018.04.101.

17 .Ovchinnikov V, Louveau J, Barton J, Karplus M, Chakraborty A. Role of Framework Mutations and Antibody Flexibility in the Evolution of Broadly Neutralizing Antibodies. *eLife* **7** (2018) 0. doi:10.7554/eLife.33038.

18 .Ellebedy A, Krammer F, Li G, Miller M, Chiu C, Wrammert J, et al. Induction of Broadly Cross-Reactive Antibody Responses to the Influenza Ha Stem Region Following H5N1 Vaccination in Humans. *Proc. Natl. Acad. Sci. USA* **111** (2014) 13133–8. doi:10.1073/pnas.1414070111.

19 .Tan H, Jegaskanda S, Juno J, Esterbauer R, Wong J, Kelly H, et al. Subdominance and Poor Intrinsic Immunogenicity Limit Humoral Immunity Targeting Influenza Ha Stem. *The J. Clin. Invest.* **129** (2019) 850–862. doi:10.1172/JCI123366.

20 .Arevalo C, Le Sage V, Bolton M, Eilola T, Jones J, Kormuth K, et al. Original Antigenic Sin Priming of Influenza Virus Hemagglutinin Stalk Antibodies. *Proc. Natl. Acad. Sci. USA* **117** (2020) 17221–17227. doi:10.1073/pnas.1920321117.

21 .Nachbagauer R, Choi A, Izikson R, Cox M, Palese P, Krammer F. Age Dependence and Isotype Specificity of Influenza Virus Hemagglutinin Stalk-Reactive Antibodies in Humans. *mBio* **7** (2016) e01996–15. doi:10.1128/mBio.01996-15.

22 .Andrews S, Huang Y, Kaur K, Popova L, Ho I, Pauli N, et al. Immune History Profoundly Affects Broadly Protective B Cell Responses to Influenza. *Sci. Trans. Med.* **7** (2015) 316ra192. doi:10.1126/scitranslmed.aad0522.

23 .Xiao X, Chen W, Feng Y, Zhu Z, Prabakaran P, Wang Y, et al. Germline-like predecessors of broadly neutralizing antibodies lack measurable binding to hiv-1 envelope glycoproteins: implications for

806 evasion of immune responses and design of vaccine immunogens. *Biochemical and biophysical*
807 *research communications* **390** (2009) 404–9. doi:10.1016/j.bbrc.2009.09.029.

808 24 .Amitai A, Sangesland M, Barnes R, Rohrer D, Lonberg N, Lingwood D, et al.   Defining and
809 Manipulating B Cell Immunodominance Hierarchies to Elicit Broadly Neutralizing Antibody Responses
810 Against Influenza Virus. *Cell Syst.* **11** (2020) 573–588.e9. doi:10.1016/j.cels.2020.09.005.

811 25 .Wang S. Optimal Sequential Immunization Can Focus Antibody Responses Against Diversity Loss
812 and Distraction. *PLoS Comput. Biol.* **13** (2017) 1–27. doi:10.1371/journal.pcbi.1005336.

813 26 .Ives S, Bürckert JP, Pettus C, Peñate K, Hovde R, Bayless N, et al. a General Solution to Broad-Spectrum
814 Vaccine Design for Rapidly Mutating Viruses. *submitted* (2020). doi:10.21203/rs.3.rs-100459/v1.

815 27 .Harris A, Meyerson J, Matsuoka Y, Kuybeda O, Moran A, Bliss D, et al. Structure and Accessibility
816 of Ha Trimers on Intact 2009 H1N1 Pandemic Influenza Virus to Stem Region-Specific Neutralizing
817 Antibodies. *Proc. Natl. Acad. Sci. USA* **110** (2013) 4592–7. doi:10.1073/pnas.1214913110.

818 28 .Kanekiyo M, Joyce M, Gillespie R, Gallagher J, Andrews S, Yassine H, et al. Mosaic Nanoparticle
819 Display of Diverse Influenza Virus Hemagglutinins Elicits Broad B Cell Responses. *Nat. Immunol.* **20**
820 (2019) 362–372. doi:10.1038/s41590-018-0305-x.

821 29 .Cohen A, Gnanapragasam P, Lee Y, Hoffman P, Ou S, Kakutani L, et al. Mosaic Nanoparticles Elicit
822 Cross-Reactive Immune Responses to Zoonotic Coronaviruses in Mice. *Science (New York, N.Y.)* **371**
823 (2021) 735–741. doi:10.1126/science.abf6840.

824 30 .Williams W, Meyerhoff R, Edwards R, Li H, Manne K, Nicely N, et al.   Fab-dimerized glycan-
825 reactive antibodies are a structural category of natural antibodies. *Cell* **184** (2021) 2955–2972.e25.
826 doi:10.1016/j.cell.2021.04.042.

827 31 .Zhang Y, Meyer-Hermann M, George L, Figge M, Khan M, Goodall M, et al. Germinal Center B Cells
828 Govern Their Own Fate Via Antibody Feedback. *J. Exp. Med.* **210** (2013) 457–64. doi:10.1084/jem.
829 20120150.

830 32 .Kepler T, Perelson A. Somatic Hypermutation in B Cells: An Optimal Control Treatment. *J. Theor.*
831 *Biol.* **164** (1993) 37–64. doi:10.1006/jtbi.1993.1139.

832 33 .Oprea M, Perelson AS. Somatic Mutation Leads to Efficient Affinity Maturation When Centrocytes
833 Recycle Back to Centroblasts. *J. Immunol.* **158** (1997) 5155–5162.

834 34 .Meyer-Hermann M.   a Mathematical Model for the Germinal Center Morphology and Affinity
835 Maturation. *J. Theor. Biol.* **216** (2002) 273–300. doi:10.1006/jtbi.2002.2550.

836 35 .Meyer-Hermann M, Mohr E, Pelletier N, Zhang Y, Victora G, Toellner K. a Theory of Germinal Center
837 B Cell Selection, division, and exit. *Cell Rep.* **2** (2012) 162–74. doi:10.1016/j.celrep.2012.05.010.

838 36 .Zhang J, Shakhnovich E. Optimality of Mutation and Selection in Germinal Centers. *PLoS Comput.*
839 *Biol.* **6** (2010) e1000800. doi:10.1371/journal.pcbi.1000800.

840 37 .Wang S, Mata-Fink J, Kriegsman B, Hanson M, Irvine D, Eisen H, et al. Manipulating the Selection
841 Forces During Affinity Maturation to Generate Cross-Reactive HIV Antibodies. *Cell* **160** (2015)
842 785–797. doi:10.1016/j.cell.2015.01.027.

843 38 .Robert P, Marschall A, Meyer-Hermann M. Induction of Broadly Neutralizing Antibodies in Germinal
844 Centre Simulations. *Curr. Opin. Biotech.* **51** (2018) 137–145. doi:10.1016/j.copbio.2018.01.006.

845 39 .Allen C, Okada T, Cyster J. Germinal-Center Organization and Cellular Dynamics. *Immunity* **27** (2007)
846 190–202. doi:10.1016/j.immuni.2007.07.009.

847 40 .Mayer A, Zhang Y, Perelson A, Wingreen N. Regulation of T Cell Expansion by Antigen Presentation
848 Dynamics. *Proc. Natl. Acad. Sci. USA* **116** (2019) 5914–5919. doi:10.1073/pnas.1812800116.

849 41 .Erwin S, Childs L, Ciupe S. Mathematical model of broadly reactive plasma cell production. *Sci. Rep.*
850 **10** (2020) 3935. doi:10.1038/s41598-020-60316-8.

42 .Wittenbrink N, Klein A, Weiser A, Schuchhardt J, Or-Guil M. Is There a Typical Germinal Center? a Large-Scale Immunohistological Study on the Cellular Composition of Germinal Centers During the Hapten-Carrier-Driven Primary Immune Response in Mice. *J. Immunol. (Baltimore, Md. : 1950)* **187** (2011) 6185–96. doi:10.4049/jimmunol.1101440.

43 .Pélissier A, Akrout Y, Jahn K, Kuipers J, Klein U, Beerenwinkel N, et al. Computational Model Reveals a Stochastic Mechanism Behind Germinal Center Clonal Bursts. *Cells* **9** (2020) 0. doi:10.3390/cells9061448.

44 .Weisel F, Zuccarino-Catania G, Chikina M, Shlomchik M. a Temporal Switch in the Germinal Center Determines Differential Output of Memory B and Plasma Cells. *Immunity* **44** (2016) 116–130. doi:10.1016/j.immuni.2015.12.004.

45 .Yan L, Wang S. Shaping polyclonal responses via antigen-mediated antibody interference. *iScience* **23** (2020) 101568. doi:https://doi.org/10.1016/j.isci.2020.101568.

46 .Turner J, Zhou J, Han J, Schmitz A, Rizk A, Alsoussi W, et al. Human germinal centres engage memory and naive b cells after influenza vaccination. *Nature* **586** (2020) 127–132. doi:10.1038/s41586-020-2711-0.

47 .Nachbagauer R, Liu W, Choi A, Wohlbold T, Atlas T, Rajendran M, et al. a Universal Influenza Virus Vaccine Candidate Confers Protection Against Pandemic H1N1 Infection in Preclinical Ferret Studies. *NPJ vaccines* **2** (2017) 26. doi:10.1038/s41541-017-0026-4.

48 .Krammer F, Pica N, Hai R, Tan G, Palese P. Hemagglutinin Stalk-Reactive Antibodies Are Boosted Following Sequential Infection with Seasonal and Pandemic H1N1 Influenza Virus in Mice. *J. Virol.* **86** (2012) 10302–7. doi:10.1128/JVI.01336-12.

49 .Eggink D, Goff P, Palese P. Guiding the Immune Response Against Influenza Virus Hemagglutinin Toward the Conserved Stalk Domain by Hyperglycosylation of the Globular Head Domain. *J. Virol.* **88** (2014) 699–704. doi:10.1128/JVI.02608-13.

50 .Zhou T, Doria-Rose N, Cheng C, Stewart-Jones G, Chuang G, Chambers M, et al. Quantification of the Impact of the HIV-1-Glycan Shield on Antibody Elicitation. *Cell Rep.* **19** (2017) 719–732. doi:10.1016/j.celrep.2017.04.013.

51 .Yassine H, Boyington J, McTamney P, Wei C, Kanekiyo M, Kong W, et al. Hemagglutinin-Stem Nanoparticles Generate Heterosubtypic Influenza Protection. *Nat. Med.* **21** (2015) 1065–70. doi:10.1038/nm.3927.

52 .Corbett K, Moin S, Yassine H, Cagigi A, Kanekiyo M, Boyoglu-Barnum S, et al. Design of Nanoparticulate Group 2 Influenza Virus Hemagglutinin Stem Antigens That Activate Unmutated Ancestor B Cell Receptors of Broadly Neutralizing Antibody Lineages. *mBio* **10** (2019) 0. doi:10.1128/mBio.02810-18.

53 .Boyoglu-Barnum S, Hutchinson G, Boyington J, Moin S, Gillespie R, Tsybovsky Y, et al. Glycan Repositioning of Influenza Hemagglutinin Stem Facilitates the Elicitation of Protective Cross-Group Antibody Responses. *Nature communications* **11** (2020) 791. doi:10.1038/s41467-020-14579-4.

54 .Garg A, Mittal S, Padmanabhan P, Desikan R, Dixit N. Increased b cell selection stringency in germinal centers can explain improved covid-19 vaccine efficacies with low dose prime or delayed boost. *Frontiers Immunol.* **12** (2021) 776933. doi:10.3389/fimmu.2021.776933.

55 .Galimidi R, Klein J, Politzer M, Bai S, Seaman M, Nussenzweig M, et al. Intra-spike crosslinking overcomes antibody evasion by hiv-1. *Cell* **160** (2015) 433–46. doi:10.1016/j.cell.2015.01.016.

56 .Keating R, Johnson J, Brice D, Labombarde J, Dent A, McGargill M. Broadly reactive influenza antibodies are not limited by germinal center competition with high-affinity antibodies. *mBio* **11** (2020) 0. doi:10.1128/mBio.01859-20.

57 .Barnes C, West A, Huey-Tubman K, Hoffmann M, Sharaf N, Hoffman P, et al. Structures of human antibodies bound to sars-cov-2 spike reveal common epitopes and recurrent features of antibodies. *Cell* **182** (2020) 828–842. doi:10.1016/j.cell.2020.06.025.

58 .Robert P, Arulraj T, Meyer-Hermann M. Ymir: A 3d structural affinity model for multi-epitope vaccine simulations. *iScience* **24** (2021) 102979. doi:10.1016/j.isci.2021.102979.

59 .Conti S, Kaczorowski K, Song G, Porter K, Andrabi R, Burton D, et al. Design of Immunogens to Elicit Broadly Neutralizing Antibodies Against HIV Targeting the CD4 Binding Site. *Proc. Natl. Acad. Sci. USA* **118** (2021) 0. doi:10.1073/pnas.2018338118.

60 .Sprenger K, Conti S, Ovchinnikov V, Chakraborty A, Karplus M. Multiscale affinity maturation simulations to elicit broadly neutralizing antibodies against hiv. *submitted, PLoS Comput. Biol.* (2021).

61 .Cohen A, Yang Z, Gnanapragasam P, Ou S, Dam K, Wang H, et al. Construction, characterization, and immunization of nanoparticles that display a diverse array of influenza ha trimers. *PloS one* **16** (2021) e0247963. doi:10.1371/journal.pone.0247963.

62 .Casten L, Pierce S. Receptor-Mediated B Cell Antigen Processing. Increased Antigenicity of a Globular Protein Covalently Coupled to Antibodies Specific for B Cell Surface Structures. *J. Immunol. (Baltimore, Md. : 1950)* **140** (1988) 404–10.

63 .Alberts B, Johnson A, Lewis J, Raf M, Roberts K, Walter P. *Molecular Biology of the Cell* (New York: Garland Science), fourth edn. (2002).

64 .Press W, Flannery B, Teukolsky S, Vetterling W. *Numerical Recipes in FORTRAN 77: The Art of Scientific Computing* (Cambridge University Press), second edn. (1992).

65 .Anderson S, Khalil A, Uduman M, Hershberg U, Louzoun Y, Haberman A, et al. Taking Advantage: High-Affinity B Cells in the Germinal Center Have Lower Death Rates, but similar rates of division, compared to low-affinity cells. *J. Immunol. (Baltimore, Md. : 1950)* **183** (2009) 7314–25. doi:10.4049/jimmunol.0902452.

66 .Gitlin A, Mayer C, Oliveira T, Shulman Z, Jones M, Koren A, et al. HUMORAL IMMUNITY. T Cell Help Controls the Speed of the Cell Cycle in Germinal Center B Cells. *Science (New York, N.Y.)* **349** (2015) 643–6. doi:10.1126/science.aac4919.

67 .Amitai A, Mesin L, Victora G, Kardar M, Chakraborty A. a Population Dynamics Model for Clonal Diversity in a Germinal Center. *Front. Microbiol.* **8** (2017) 1693. doi:10.3389/fmicb.2017.01693.

68 .Hill TL. *an Introduction to Statistical Thermodynamics* (New York: Dover) (1986).

69 .El Shikh M, El Sayed R, Sukumar S, Szakal A, Tew J. Activation of B Cells by Antigens on Follicular Dendritic Cells. *Trends. Immunol.* **31** (2010) 205–11. doi:10.1016/j.it.2010.03.002.

70 .Saphire E, Parren P, Pantophlet R, Zwick M, Morris G, Rudd P, et al. Crystal Structure of a Neutralizing Human IGG Against HIV-1: A Template for Vaccine Design. *Science (New York, N.Y.)* **293** (2001) 1155–9. doi:10.1126/science.1061692.

71 .Ise W, Kurosaki T. Plasma Cell Differentiation During the Germinal Center Reaction. *Immunol. Rev.* **288** (2019) 64–74. doi:10.1111/imr.12751.

72 .Rundell A, DeCarlo R, HogenEsch H, Doerschuk P. the Humoral Immune Response to Haemophilus Influenzae Type B: A Mathematical Model Based on T-Zone and Germinal Center B-Cell Dynamics. *J. Theor. Biol.* **194** (1998) 341–81. doi:10.1006/jtbi.1998.0751.

73 .Kelsoe G. *in Situ* studies of the germinal center reaction. *Adv. Immunol.* **60** (1995) 267–288.

74 .Murphy K. *Janeway's Immunobiology* (New York: Garland Science), eighth edn. (2012).

75 .Liu Y, Johnson G, Gordon J, MacLennan I. Germinal Centres in T-Cell-Dependent Antibody Responses. *Immunol. Today* **13** (1992) 17–21. doi:10.1016/0167-5699(92)90199-H.

940 **76** .Leanderson T, Källberg E, Gray D. Expansion, selection and mutation of antigen-specific b cells in
941   germinal centers. *Immunol. Rev.* **126** (1992) 47–61. doi:10.1111/j.1600-065x.1992.tb00630.x.

942 **77** .Eaton JW, Bateman D, Hauberg S, Wehbring R. *GNU Octave Version 4.0.0 Manual: A High-Level*
943   *Interactive Language for Numerical Computations* (2015).

944 **78** .Moin P. *Fundamentals of Engineering Numerical Analysis* (Cambridge University Press) (2001).

FIGURE CAPTIONS

Figure . 1. Influenza hemagglutinin (HA) spike protein colored by residue conservation. Sequences of avian, swine and human influenza type A spike proteins spanning the years 1918–2019 and subtypes 1-18 were downloaded from the NIH influenza research database(3); conservation was computed in MATLAB(4) after clustering the sequences to 97% identity and multiple alignment. The HA structure was taken from PDB entry 3LZG(5), and the image was generated using Visual Molecular Dynamics.(6) Only the C_α atoms are shown.

Figure . 2. Schematic of the GC model used in this study. (A) Model overview: (1) B-cells are activated upon binding to antigen presented on follicular dendritic cells (FDCs, not explicitly modeled); (1a) in the optional T-cell help model (see text) B-cells are activated when the major histocompatibility complex receptor (MHC2) binds to the T-cell receptor (TCR); B-cell activation rescues B-cells from apoptosis, allowing them to mutate and proliferate; (2) depending on the activation signal, B-cells can differentiate to plasma cells (2a), to memory B-cells (2b), or undergo apoptosis (2c); (3) Plasma cells secrete antibodies (Abs), which also compete with B-cell receptors for antigen (4), which is the essential aspect of the Ab feedback model(31) (see text). (B) Hypothetical modes of antibody binding to influenza spikes; bivalent binding without strain (top) corresponds to cooperative binding by antibody arms; bivalent binding with strain (middle) corresponds to noncooperative binding; monovalent binding (bottom) is assumed to be the dominant mode of binding of anti-HA stem antibodies (see Methods for details).

Figure . 3. Comparison of simulation and experiments. A: Total B-cells, B: Memory B-cell production rate, C: Plasma cell production rate. Experimental data for panel A was generated from the GC cross-sectional areas plotted in Fig. S1B of Ref. 42, and converted to B cell counts as done in Ref. 43; The lower and upper error bars in panel A corresponds to 30% and 70% quantiles, respectively ; experimental data for panels B & C was taken from Fig. 4 of Ref. 43, who obtained raw data from Weisel et al. (44); the error bars in B & C correspond to approximately one SD.

Figure . 4. Effect of antibody valency and epitope occlusion on GC properties. Left column (A–C): noninteracting B-cell case ($o = 0$); Right column (D–F): fully interacting B-cell case ($o = 1$); A,D: Total B cells; B,E: Memory cell production rate; insets: total MBC population at end of simulation; C,F: Average affinity of B-cells and MBCs. For the definition of occlusion o, see Sec. 4.0.5.

Figure . 5. Effect of initial affinity advantage on the growth of monovalent B-cells in the fully interacting B-cell case ($o = 1$). Panels A–C show the same quantities as Fig. 4A–C; The affinity distribution corresponding to BCR#1 was shifted toward higher values relative to BCR#2 and BCR#3 (panel D).

Figure . 6. Fraction of MBC#1 (ζ, defined in the text) at the end of six GC simulations for different initial affinity advantage values *vs.* total number of BCR/Epitope pairs. A: BCR#1 is cooperatively bivalent ($K_{eq}^{12}=10K_{eq}^{11}$); B: BCR#1 is monovalent ($K_{eq}^{12}=0$).

Figure . 7. Effect of BCR valency and epitope concentration on GC evolution, with $o = 1$ (fully competitive case). Panels A–C show the same quantities as Fig. 4A–C; $\alpha_1^T = 2$, $\alpha_2^T = 1$, $\alpha_3^T = 1$; α^T is the nondimensional AG concentration (see Sec. 4.0.6).

Figure . 8. Fraction of MBC#1 *vs.* number of sequential GC simulations for different initial affinity advantage values and different AG#1 concentrations, with 10 total BCR/Epitope pairs. A & B: MBC#1 fraction (ζ) at the end of simulations. A: BCR#1 is cooperatively bivalent ($K_{eq}^{12}=10K_{eq}^{11}$); B: BCR#1 is monovalent ($K_{eq}^{12}=0$). The four sets of panels A and B show the effect of increasing occlusion from $o=0$ (no competition) to $o=1$ (full competition).

CONTRIBUTION TO THE FIELD

945 Viral pathogens such as influenza, coronavirus, and HIV remain a high source of global mortality and
946 morbidity, because their rapid rate of mutation presents serious challenges to vaccine design. Many anti-
947 viral vaccines are currently in development, but to be effective against future strains, they must raise
948 host immunity to structurally conserved regions of the virus. Unfortunately, viral adaptation conceals
949 such conserved epitopes from the immune system and guides host immunity towards highly variable,
950 distracting epitopes. Success in developing vaccines against rapidly mutating viruses depends critically on
951 understanding and learning how to overcome this distraction. We have developed and validated a computer
952 model of adaptive immunity, in which we simulate the development of high-affinity antibodies to antigenic
953 epitopes with different properties. We find that the mode of antibody binding to antigens can explain
954 experimental results that show that the immune system is easily directed from certain conserved epitopes
955 toward variable ones. We performed additional simulations to explore the influence of antigen concentration
956 on the competition between different antibodies, and whether raised immunity to conserved (but concealed)
957 epitopes could be long lasting. Our results are expected to inform design of universal vaccines.